| OF |
AD
A046504

END
DATE
FILMED

12-77

DDC

1.0

1.1

1.25 1.4 1.6

4.5
5.0
5.6

2.8 2.5

3.2 2.2

3.6

4.0 2.0

1.8

MICROCOPY RESOLUTION TEST CHART

NATIONAL BUREAU OF STANDARDS-1963
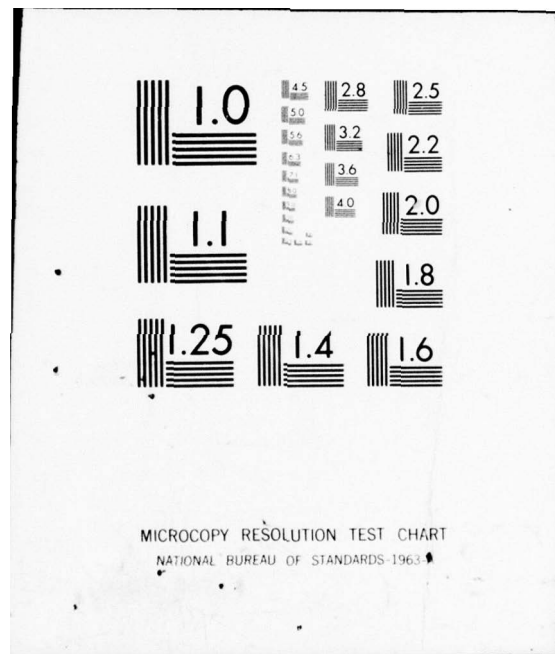
NAVAL POSTGRADUATE SCHOOL
Monterey, California
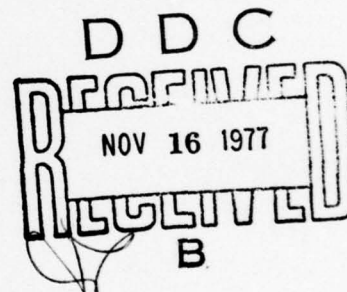
THESIS

NUMERICAL SIMULATION OF FLOW
OVER MOUNTAINS USING A CHANNELED
AND NESTED GRID MODEL

by

Stephen Michael Schrobo

September 1977

Thesis Advisor: R. L. Elsberry

Approved for public release; distribution unlimited.

REPORT DOCUMENTATION PAGE		READ INSTRUCTIONS BEFORE COMPLETING FORM
1. REPORT NUMBER	2. GOVT ACCESSION NO.	3. RECIPIENT'S CATALOG NUMBER
4. TITLE (and Subtitle) Numerical Simulation of Flow Over Mountains Using a Channeled and Nested Grid Model.		5. TYPE OF REPORT & PERIOD COVERED Master's Thesis, September 1977
		6. PERFORMING ORG. REPORT NUMBER
7. AUTHOR(s) Stephen Michael Schrobo		8. CONTRACT OR GRANT NUMBER(s)
9. PERFORMING ORGANIZATION NAME AND ADDRESS Naval Postgraduate School Monterey, California 93940		10. PROGRAM ELEMENT, PROJECT, TASK AREA & WORK UNIT NUMBERS
11. CONTROLLING OFFICE NAME AND ADDRESS Naval Postgraduate School Monterey, California 93940		12. REPORT DATE September 1977
		13. NUMBER OF PAGES 71
14. MONITORING AGENCY NAME & ADDRESS(if different from Controlling Office) Naval Postgraduate School Monterey, California 93940		15. SECURITY CLASS. (of this report) Unclassified
		15a. DECLASSIFICATION/DOWNGRADING SCHEDULE

16. DISTRIBUTION STATEMENT (of this Report)

Approved for public release; distribution unlimited.

17. DISTRIBUTION STATEMENT (of the abstract entered in Block 20, if different from Report)

18. SUPPLEMENTARY NOTES

19. KEY WORDS (Continue on reverse side if necessary and identify by block number)

20. ABSTRACT (Continue on reverse side if necessary and identify by block number)

A channeled model with a fine resolution nested grid is used to study the flow over a mountain range. The basic primitive equation model is frictionless and adiabatic, with no vertical shear. The nesting is accomplished using a scheme C staggered grid arrangement. The solutions are obtained for three categories: a) coarse mesh solution, b) uniform fine mesh solution, and c) nested solution. Compari-

DD FORM 1473 1 JAN 73

EDITION OF 1 NOV 65 IS OBSOLETE
S/N 0102-014-6601 |

(Page 1)

251450   1

sons are made between solutions first with no mountain present, then with a mountain. During the early stages of the integration, the nested grid solution is improved over the coarse mesh solution. Difficulties arise at the boundaries, though, in both the coarse and fine meshes. Detailed discussions relating to these problems are presented, with suggestions on alternative boundary conditions.

ACCESSION for

NTIS	White Section
DDC	Buff Section ☐
UNANNOUNCED	☐
JUSTIFICATION	

BY
DISTRIBUTION/AVAILABILITY CODES
Dist.	AVAIL. and/or SPECIAL
A	

Approved for public release; distribution unlimited.

Numerical Simulation of Flow
Over Mountains Using a Channeled
and Nested Grid Model

by

Stephen Michael Schrobo
Lieutenant, United States Navy
B.S., New York University, 1969

Submitted in partial fulfillment of the
requirements for the degree of

MASTER OF SCIENCE IN METEOROLOGY AND OCEANOGRAPHY

from the
NAVAL POSTGRADUATE SCHOOL
September 1977

Author _____

Approved by: _____
                                        Thesis Advisor

             _____
                    Chairman, Department of Meteorology

             _____
                         Dean of Science and Engineering

3

ABSTRACT

A channeled model with a fine resolution nested grid is used to study the flow over a mountain range. The basic primitive equation model is frictionless and adiabatic, with no vertical shear. The nesting is accomplished using a scheme C staggered grid arrangement. The solutions are obtained for three categories: a) coarse mesh solution, b) uniform fine mesh solution, and c) nested solution. Comparisons are made between solutions first with no mountain present, then with a mountain. During the early stages of the integration, the nested grid solution is improved over the coarse mesh solution. Difficulties arise at the boundaries, though, in both the coarse and fine meshes. Detailed discussions relating to these problems are presented, with suggestions on alternative boundary conditions.

TABLE OF CONTENTS

LIST OF FIGURES

LIST OF SYMBOLS AND ABBREVIATIONS

a	Earth's radius
B	Arbitrary constant in stream function
c_p	Specific heat for dry air at constant pressure
F_ε	Frictional stress (zonal)
F_η	Frictional stress (meridional)
f	Coriolis parameter
g	Gravitational acceleration
H	Scale height of atmosphere
I	Zonal index
J	Meridional index
M	Height of mountain
m	$\dfrac{1}{a\ \cos\ \phi}$
mb	Millibars
n	$\dfrac{1}{a}$
p	Pressure
p_s	Surface pressure
p_t	Constant pressure at top of numerical model
p_o	1000 mb
Q	Moisture source or sink term
R	Specific gas constant for dry air
t	time
t_p	Length of period over which topography is introduced into the numerical model
T	Temperature
u	Zonal component of wind

v	Meridional component of wind
$\hat{V}$	Velocity vector
α	Specific volume
β	Derivative of Coriolis parameter with respect to the meridional coordinate
η	Meridional coordinate of the curvilinear coordinate system
θ	Potential temperature
κ	R/c_p
λ	Longitude
λ_R	Rossby radius of deformation
ξ	Zonal coordinate of the curvilinear coordinate system
σ	Dimensionless vertical coordinate
$\dot{\sigma}$	Measure of vertical velocity
Φ	Geopotential
Φ_{sfc}	Geopotential of the lower boundary of the numerical model
ϕ	Latitude
ψ	Stream function
Ω	Angular velocity of the earth

ACKNOWLEDGEMENT

I. INTRODUCTION

The effects of mountain ranges on synoptic scale motions have been shown (Reiter, 1971) to be quite influential. Yet, the physical cause and mathematical description of these effects are poorly understood. The large-scale flow over and around mountain ranges is not properly observed or mathematically well modeled. This was quite evident to this author, having spent three years of forecasting weather for the European-Mediterranean area, where the Alps, Pyrenees, and other mountain ranges have a marked meteorological effect. Due to the grid size of most primitive equation models, a nested, finer resolution grid is required to depict accurately the flow over and around mountains. This is attempted in this study.

The general circulation model used in this study is a modified version (Monaco, 1975) of the UCLA global prediction model. To reduce computer memory and run-time requirements prior to nesting a finer resolution grid, a channeling of the global model was undertaken. Procedures had to be developed to take into account the scheme C (Monaco, 1975) grid arrangement of the model and the higher order form of the flux terms in the primitive equations.

In nesting a fine resolution scheme C grid, certain conditions had to be considered to take into account the staggered grid arrangement. Unlike the majority of nested grid

models presently available which use unstaggered grid arrangements, the indexing scheme used for each variable must be considered in determining interface boundary conditions.

The solutions obtained are divided into three categories: a) coarse mesh solution, b) uniform fine mesh solution, and c) nested solution. Comparisons are made between solutions with no mountain present, and then with a mountain. It is shown that a number of problems remain for the type of channeling and nesting used in the present model.

II.   MODEL DESCRIPTION AND INITIALIZATION PROCEDURES

The general circulation model used in this research has been described by Monaco and Williams (1975). It is a modified version of the UCLA global prediction model detailed by Arakawa and Mintz (1974). Our model assumes the atmosphere is adiabatic and frictionless and contains no sink or source terms. Numerical integration is carried out on a staggered, spherical, sigma coordinate system.

A. VERTICAL COORDINATE

The vertical coordinate used in the model is the non-dimensional σ-coordinate, fig. 1. It is defined as follows:

$$\sigma = \frac{p - p_t}{\pi} \tag{2.1}$$

$$\pi \equiv p_s - p_t$$

where π is the terrain pressure. The pressure is given by p, the surface pressure by p_s, and the constant tropopause pressure by p_t. The vertical boundaries of the coordinate system, the earth's surface and the constant tropopause pressure level, follow from (2.1), such that:

$$\sigma = 0 \quad \text{at} \quad p = p_t \ (= 200 \text{ mb})$$

$$\sigma = 1 \quad \text{at} \quad p = p_s \ .$$

13

The boundary condition at the tropopause pressure level, and at the earth's surface, is: $\dot{\sigma}(\equiv \frac{d\sigma}{dt}) = 0$.

B. HORIZONTAL DISTRIBUTION OF VARIABLES

The dispersion of local accumulations of wave energy generated by gravity-inertia waves is an important process in any atmospheric numerical model. Winninghoff (1968) showed how this geostrophic adjustment depended on the distribution of variables over the grid points. Five possible distributions of the dependent variables ϕ, T, v, and u are shown in fig. 2. The original UCLA general circulation model, described by Arakawa and Mintz (1974), used scheme B for the horizontal distribution of variables; this research model uses scheme C.

Winninghoff showed that schemes B and C, in a one-dimensional case, adequately simulated geostrophic adjustment. However, in a two dimensional case, scheme C was shown to be the best lattice to simulate the geostrophic adjustment process. In using scheme C, though, two conditions can cause problems. The first is due to the two velocity components not being carried at the same latitude, causing some difficulty with Coriolis force terms. The assumption of a constant Coriolis parameter could eliminate this problem. The second problem occurs if $\lambda_{R/d}$ is less than or close to one. The quantity λ_R , the Rossby radius of deformation, is given by

$$\lambda_R = \sqrt{gH} / \bar{\bar{f}}$$

14

where H is the mean value of h , the depth of the atmosphere. The situation where $\lambda_{R/d} \leq 1$ is rare and, therefore, scheme C is used.

C. PRIMITIVE EQUATIONS

The primitive equations are written using the orthogonal curvilinear coordinates, ξ and η , where $\xi = \lambda$ (longitude) and $\eta = \phi$ (latitude). Scaling factors, m and n , are defined as follows:

$$\frac{1}{m} = a \cos \phi \quad \text{and} \quad \frac{1}{n} = a .$$

The horizontal velocity components, temperature, and surface pressure, the prognostic variables, are governed by the following primitive equations:

$$\frac{\partial}{\partial t}(\frac{\pi}{mn} u) + \frac{\partial}{\partial \xi}(\frac{\pi u}{n} u) + \frac{\partial}{\partial \eta}(\frac{\pi v}{m} u) + \frac{\partial}{\partial \sigma}(\frac{\pi \dot{\sigma}}{mn} u) \qquad (2.2)$$

$$- [\frac{f}{mn} + (v \frac{\partial}{\partial \xi} \frac{1}{n} - u \frac{\partial}{\partial \eta} \frac{1}{m})] \pi v + \frac{\pi}{n}[\frac{\partial \phi}{\partial \xi} + \sigma \alpha \frac{\partial \pi}{\partial \xi}] = \frac{\pi}{mn} F_\xi ,$$

$$\frac{\partial}{\partial t}(\frac{\pi}{mn} v) + \frac{\partial}{\partial \xi}(\frac{\pi u}{n} v) + \frac{\partial}{\partial \eta}(\frac{\pi v}{m} v) + \frac{\partial}{\partial \sigma}(\frac{\pi \dot{\sigma}}{mn} v) \qquad (2.3)$$

$$+ [\frac{f}{mn} + (v \frac{\partial}{\partial \xi} \frac{1}{n} - u \frac{\partial}{\partial \eta} \frac{1}{m})] \pi u + \frac{\pi}{m}[\frac{\partial \phi}{\partial \eta} + \sigma \alpha \frac{\partial \pi}{\partial \eta}] = \frac{\pi}{mn} F_\eta ,$$

$$\frac{\partial}{\partial t}(\frac{\pi}{mn} c_p T) + \frac{\partial}{\partial \xi}(\frac{\pi u}{n} c_p T) + \frac{\partial}{\partial \eta}(\frac{\pi v}{m} c_p T)$$

$$+ (\frac{p}{p_o})^\kappa \frac{\partial}{\partial \sigma}(\frac{\pi \dot{\sigma}}{mn} c_p \theta) \qquad (2.4)$$

$$= \pi \sigma \alpha [\frac{\partial}{\partial t}(\frac{\pi}{mn}) + \frac{u}{n} \frac{\partial \pi}{\partial \xi} + \frac{v}{m} \frac{\partial \pi}{\partial \eta}] + \frac{\pi}{mn} Q ,$$

15

and

$$\frac{\partial}{\partial t}(\frac{\pi}{mn}) + \frac{\partial}{\partial \xi}(\frac{\pi u}{n}) + \frac{\partial}{\partial \eta}(\frac{\pi v}{m}) + \frac{\partial}{\partial \sigma}(\frac{\pi \dot{\sigma}}{mn}) = 0 \ , \tag{2.5}$$

$$\alpha = \frac{RT}{p} \tag{2.6}$$

$$\delta \Phi = -\pi \alpha \delta \sigma \ . \tag{2.7}$$

A complete listing of the symbols used in the preceding equations may be found in the front of this report.

The vertical σ-velocity is given by:

$$\pi \dot{\sigma} = - \int_{o}^{\sigma} \nabla \cdot (\pi \dot{V}) d\sigma - \sigma \frac{\partial}{\partial t}(\frac{\pi}{mn}) \ . \tag{2.8}$$

In determining geopotentials, conservation of total energy under adiabatic and frictionless processes, and conservation of θ and lnθ, integrated over the entire mass under adiabatic processes, are needed. In addition, the vertical difference scheme must maintain the property of the vertically integrated horizontal pressure gradient force. This is achieved essentially by combining an alternate form of the hydrostatic equation, written in terms of potential temperature (2.9), with the vertical integral of hydrostatic equation (2.10):

$$\partial \Phi = c_p \frac{d \ln \theta}{d(\frac{1}{\theta})} \partial (\frac{p}{p_o})^\kappa \ , \tag{2.9}$$

$$\int_{o}^{1} d(\Phi \sigma) = - \int_{o}^{1} (\pi \sigma \alpha - \Phi) d\sigma \ . \tag{2.10}$$

16

The system is complete when the above two diagnostic equations are included with the primitive equations.

D. ANALYTIC INITIALIZATION

The initial wind and pressure (geopotential) fields are defined mathematically in this model which has some advantages over obtaining the fields from a weather map. The analytic initial conditions: 1) simplify the task of interpolating and balancing initial fields from constant pressure surfaces to sigma surfaces, 2) minimize imbalances between wind and pressure fields thereby reducing gravity-inertia waves.

Haurwitz (1940), in defining the initial velocity fields, solved the linearized, non-divergent vorticity equation for the stream function. The initial distribution of geopotential was obtained by using this solution in the forcing function of the non-linear balance equation (Phillips, 1959).

Initialization of the model, based on the aforementioned solutions, was achieved using the following equations:

$$\psi = -Ba^2 \sin \phi$$

$$\phi' = a^2 A(\phi)$$

$$u = -\frac{1}{a} \frac{\partial \psi}{\partial \phi} = Ba \cos \phi \qquad (2.11)$$

$$v = \frac{1}{a \cos \phi} \frac{\partial \psi}{\partial \lambda} = 0 \ ,$$

where $\qquad A(\phi) = \frac{1}{2} (2\Omega + B)B \cos^2 \phi \ .$

17

These equations represent solid rotation of the atmosphere
because of the absence of vertical wind shear. The horizon-
tal or zonal wind distribution varies as the cosine of the
latitude and the magnitude of the constant, B. The zonal
wind distribution in the model varied from $u = 15.2$ m-sec^{-1}
at 34°N to $u = 13.8$ m-sec^{-1} at 58°N. The initial tempera-
ture field was determined in accordance to the NACA standard
atmosphere as defined by Haltiner and Martin (1957).

E. PROCEDURE FOR INTRODUCING TOPOGRAPHY INTO MODEL

The scheme used to introduce mountain topography into
the model is described in detail by Hayes (1977). Initially,
heights at the surface were set equal to zero everywhere.
During the model integration, the heights of the mountain
grid points were increased as a function of time until the
desired heights were achieved. The problem with wind field
initialization in the vicinity of the mountain precluded
starting with a mountain "already built". The following
equations were used at the mountain grid points:

$$\Phi_{sfc} \begin{cases} = M \sin^2 \left(\frac{\pi t}{2t_p}\right) , & t \le t_p \\ = M , & t > t_p \end{cases} \tag{2.12}$$

where Φ_{sfc} is the geopotential height at time t, M is
the final geopotential mountain height, and t_p is the
period of mountain "building". Values used in this research
are:

$$\Phi_{sfc(max)} = 7500 \text{ gpm} ,$$
$$t_p = 12 \text{ hours} .$$

III. CHANNELING THE COARSE GRID MODEL

In any numerical modeling, considerations of computer run-times and memory requirements are necessary. This is especially true when developing and testing fine mesh grids where the grid spacing, and therefore the time step, are small. With this in mind, an attempt to channel the global prediction model (Arakawa, 1972; Arakawa and Mintz, 1974; Monaco and Williams, 1975) in the north-south direction was made prior to nesting of a finer resolution grid.

A. PROCEDURES FOR CHANNELING

In the initial phase of this research, the assumption of no variation in the north-south (η) direction was considered. This led to reducing the amount of north-south pressure grid points in the model from 46 to 7. In accomplishing this, the pole modification schemes for the various predictive equations were eliminated.

In addition to removing the smoothing effect of the pole modifications, the effect of another scheme which zonally smooths the ξ-components of the pressure gradient force and the divergence was reduced. This zonal smoothing eliminates computational instabilities due to the convergence of meridians at the pole. This smoothing is a function of latitude, grid size, and wave number; therefore, due to the channel being centered at 46°N with a width of only 8° latitude, its effect was much reduced.

Although the above routines might have had a damping influence on some of the large variations encountered with the model, the elimination or reduction of these routines did not generate any oscillations. Rather, these oscillations were generated by the channel boundary conditions.

B. BOUNDARY CONDITIONS

Simple cyclic conditions east-west were used, but the north-south boundary conditions proved to be quite formidable. The main constraint, for the north-south direction, was that of no net mass flux in the η-direction. The two main problems in this regard were the balancing of pressure gradient term to the u-velocity component and the integrated mass flux in the η-direction. Compounding the problem further were the scheme C grid arrangement and the complex flux forms of the advective terms in the equation of motion.

The scheme C grid point did not allow easy selection of the boundary walls, due to the asymmetry of the variables at each (I,J) grid point. The flux terms of the advective equations involved a second order Jacobian scheme which required specification of some terms outside the walls. These problems were implicitly inherent in all boundary considerations.

For the constraint of no mass flux in the north-south direction to be achieved, the v-equation of motion, (2-3), integrated in the vertical and ξ-directions must balance. The three terms that must be specifically dealt with along the boundaries are the integrated pressure gradient, normal

component of mass flux, and Coriolis terms. (Details are given in Appendix A.)

The method used to prevent net mass flux across the walls was to reflect the normal component of the mass flux from the immediate interior grid point by one opposite in sign but equal in magnitude just outside the wall. This was accomplished by the following equations:

$$(\pi v \frac{\Delta \xi}{m})_{I,2} + (\pi v \frac{\Delta \xi}{m})_{I,1} = 0 \qquad (3\text{-}1)$$

$$(\pi v \frac{\Delta \xi}{m})_{I,Jmax} + (\pi v \frac{\Delta \xi}{m})_{I,Jmax+1} = 0 . \qquad (3\text{-}2)$$

The term $(\pi v \frac{\Delta \xi}{m})_{I,Jmax+1}$ is a mass flux quantity outside the boundary wall, which was needed in the advective terms of the equations of motion.

Although this procedure assured no mass flux across each boundary, it did not assure zero net mass flux over the entire field. This is due to the inequality between the northern and southern mass flux terms, i.e.:

$$(\pi v \frac{\Delta \xi}{m})_{I,1} + (\pi v \frac{\Delta \xi}{m})_{I,Jmax+1} \neq 0 . \qquad (3\text{-}3)$$

This imbalance did contribute to total field mass variations with time.

Along the walls the balance between the pressure gradient and the geostrophic u-component,

$$\frac{f\pi}{mn} u = - \frac{\pi}{m} [\frac{\partial \phi}{\partial \eta} + \sigma \alpha \frac{\partial \pi}{\partial \eta}] , \qquad (3\text{-}4)$$

21

was difficult to mainta'n. The gradient of terrain pressure, $\frac{\partial \pi}{\partial \eta}$, was restored to its initial value after each time step. This allowed the pressure to. vary along the walls, but maintained the initial pressure gradient. The geopotential height gradient was controlled in a different way. Since geopotential height fields are not stored but calculated at every time step, restoring the gradient $\frac{\partial \phi}{\partial \eta}$ to its initial value was not straightforward.

The method used to s ecify $\frac{\partial \phi}{\partial \eta}$ was through the parameters that ϕ was a function of, i.e. temperature, pressure, and, indirectly, the velocity components. Since the boundary grid points were not predictive points, the values needed at the boundary walls were provided by extrapolation schemes using interior predictive values. Since $\frac{\partial \phi}{\partial \eta} = 0$ at $\sigma = 1$, but increases with elevation as $\sigma \alpha \frac{\partial \pi}{\partial \eta}$ decreases, any imbalance in the parameters used to control ϕ become more significant with height. With or without a mountain in the model, the largest variation of the v-component always occurred at sigma level 1 and decreased downward. This was evidently due to the large $\frac{\partial \phi}{\partial \eta}$ term in the v-component equation.

With the inequality of normal mass flux terms plus the imbalance in the boundary zonal flow, there was a variation in the total field mass, and the oscillations were evident in the surface pressure fields. This variation of pressure along the north-south direction with time is shown in Fig. 3. The approximate period of the oscillations is 20 hours, which indicates that the forcing might originate from the southern

22

boundary where the inertial period is 21.5 hours. This might indicate a net mass inflow from the south in the early stages.

One attempt was made to eliminate these pressure, i.e. mass, variations. The change in terrain pressure between two time steps, averaged over the entire grid, was subtracted from the forecast pressure fields. As shown in Fig. 3, this reduced the oscillations substantially but, as shown in Fig. 4, caused an increase in the temperature variation. This temperature increase then caused problems in the calculation of geopotential heights along the boundaries. The procedure was discarded, thereby allowing net mass changes over the entire field to occur.

The phase and period of these pressure oscillations were dependent on the grid and domain size. The oscillations in a model with a grid distance of 4° latitude versus 1.5° latitude are compared in Fig. 5. In addition, the domain size of the 1.5° latitude grid is one-third that of the 4° latitude grid. The phase shift of six hours between the two grid spacing is obvious, but there is also a slight period change. The smaller grid has a period of approximately 18 hours. This is the inertial period for the southernmost run which adds evidence that the mass variations are forced from the south.

C. GRID ARRANGEMENT AND ADVECTIVE TERMS

As mentioned in the preceding section, the scheme C grid arrangement and the complex form of the advective terms

compounded the problems at the boundary walls. The following is a brief description of these problems.

1. <u>Scheme C Grid Arrangement</u>

In Figs. 6A and 6B the parameters enclosed by a triangle comprise a scheme C (I,J) grid point. This indexing nomenclature lends itself readily to placing a boundary wall not at one latitude but two. This was used in this research, and proved to cause more problems than it solved.

Since the boundary walls are not predictive points, values of π , T , U , V must be provided to allow time stepping of the interior points. As discussed in section B, the extrapolated methods used in this research were not completely satisfactory. An example of this is the divergence calculation at π-point (I+1, Jmax-1). The $\frac{\partial(\pi u)}{\partial \xi}$ term is based completely on predictive values, where the $\frac{\partial(\pi v)}{\partial \eta}$ term is not. Since the same gradient of π and V is maintained between (Jmax-1, Jmax-2) and (Jmax, Jmax-1), an artificiality could develop with the presence of a disturbance along the boundary. As long as an indexed (I,J) grid point is used as a channel wall, this problem will exist.

An alternative channel wall boundary was considered, but not tried. It was to have had an unequal number of rows between the parameters U , ϕ , T , π , $\dot{\sigma}$ and V in the north-south direction. This would allow the U , ϕ , T , π latitude row to be predictive along both the north and the south boundaries. This would also eliminate the problems of imbalances caused by the use of extrapolation methods for providing values at the walls. Indexing does

24

become much more complicated, though, and this was the primary reason it was not attempted.

2. Flux Form of the Advective Terms

The prevention of non-linear instabilities in a non-divergent flow can be achieved by conserving the mean square vorticity, and mean kinetic energy with time. The global model used in this thesis was written to simulate slowly changing quasi-geostrophic motion. Prevention of non-linear instability called for a second order finite difference Jacobian. This second-order Jacobian was used by Arakawa (1974) to write the non-linear advective terms of the primitive equations. Due to its second-order nature, the mass flux expression for a specific grid point required advective mass flux terms as far away as two (I,J) grid points. This presents a problem as the boundary is approached by requiring the specification of extra mass flux terms outside of the channel wall (line Jmax+1 in Fig. 6A).

The value of the normal mass flux outside the channel wall is a reflected value of Jmax. The mass flux at Jmax, though, is an extrapolated value and not a predictive value. This is due to the scheme C grid arrangement and choice of location of the channel wall. At the southern channel wall, a predictive mass flux quantity at J=2 is reflected out to J=1.

If the channel wall is placed at the latitude row having ϕ , T , π , U , and $\dot{\sigma}$, then a simplified flux scheme would be required. Although no extra flux terms would be needed for predicting temperature, another external $(\pi u \frac{\Delta \eta}{\eta})$

25

term would be needed at J=0 and J=Jmax+1 to calculate momentum flux centered on a U point (Fig. 6B). It would probably be adequate to simply set the following:

$$(\pi u \frac{\Delta \eta}{n})_{I,0} - (\pi u \frac{\Delta \eta}{n})_{I,1} = 0$$

$$(\pi u \frac{\Delta \eta}{n})_{I,Jmax} - (\pi u \frac{\Delta \eta}{n})_{I,Jmax+1} = 0 \ .$$

To briefly summarize, the scheme C grid arrangement and indexing readily leads to certain boundary wall conditions. These proved to be unsatisfactory, due to extrapolation techniques for providing the channel wall values. Another channel wall scheme was presented which would eliminate extrapolating values to the wall. However, with the integrated mass flux in the η direction not being zero, with the changing of the flux scheme for the advective terms, and with the large indexing problems, this scheme can still create difficulties. Time did not permit attempting the latter scheme.

IV.   NESTED MODEL

A.   SCHEME C NESTING

The nested grid used in this thesis consisted of two
uniform grids with the fine mesh grid centered in the chan-
neled coarse mesh grid (Fig. 7). Due to the scheme C stag-
gered grid arrangement, the ratio of the coarse mesh length
to the fine mesh length is three to one, which corresponds
to a reduction of latitude spacing of 444 km to 148 km at
the center latitude. The longitude reduction is from 348 km
to 116 km, also at the center latitude. The total number of
grid points in the coarse mesh for one sigma level is 20 x 7,
while in the fine mesh it is 19 x 7.

Although the fine mesh grid is placed at the center of
the coarse mesh, there is a minimum number of J rows required
to the north and south of the nested grid to allow inter-
action between the grids at predictive points. Due to the
extrapolation schemes used at the coarse mesh boundaries, at
least two J rows are needed to the north and south of the
nested grid. If the channel walls are changed to consist
only of the ϕ , π , T , U latitude row, then this require-
ment would be unnecessary.

The physics of the model for the nested fine mesh are
identical to those of the coarse mesh domain. The only
difference between grids was the complete elimination of the
zonal smoothing routine used in the coarse mesh.

27

B. BOUNDARY CONDITIONS

There are numerous approaches for specifying the interface boundary conditions in a nested grid model (Ookochi, 1972; Harrison and Elsberry, 1972; Chen, 1973; Moss and Jones, 1973; Chen and Miyakoda, 1974; Jones, 1976; Madala, 1977; and Miyakoda and Rosati, 1977). They range from interpolation schemes to using the finite difference equations in providing the various boundary values. The method used in this paper was the Dirichlet condition with local boundary smoothing (Chen and Miyakoda, 1974).

The boundary points are provided all necessary values of U , V , π , and T for both one and two way interaction approaches from the solutions of the coarse mesh grid. These boundary values vary with time as the coarse mesh advances in time. Linear interpolations in time and space are provided for the fine grid where necessary. Due to the flux form of the advection terms, additional mass flux terms $(\pi v \frac{\Delta \xi}{m})$ and $(\pi u \frac{\Delta \eta}{n})$ are required outside the interface. These values are also interpolated from the coarse mesh.

As described by Chen (1973) and Chen and Miyakoda (1974), this method of providing all variables at the boundary is an overspecification. This can cause a computational mode to develop at the boundaries. A method to reduce this computational mode, but not to suppress significantly the physical mode is to apply a local smoother to all variables at the grid points next to the boundaries. Chen and Miyakoda (1974) suggested the use of a simple filter (1-2-1) applied normal

28

to the boundary at the adjacent row. In this research a five point filter was used to help suppress lateral waves along the boundaries. For example, the smoothing routine for the U-component at the west boundary is as follows:

$$U_{2,J}(\text{smoothed}) = \frac{1}{2} U_{2,J} + \frac{1}{8}(U_{1,J}+U_{2,J}+U_{2,J+1}+U_{2,J-1}) \ .$$

This filter was not applied after every time step, but after every 6-3-3-3 time steps (Fig. 8).

As with the coarse mesh boundary conditions, the scheme C grid arrangement and flux forms of the advective terms affected the choice of the interface walls. A scheme C (I,J) grid point was used for the interface walls. In Fig. 7 the points surrounded by the box are predictive points, whereas fine mesh lines, I, J, I+9, J+6 are interface, non-predictive points.

Unlike the channeled coarse mesh grid, there are no conservation of mass or energy requirements for the nested fine mesh. Therefore, free exchange across the interface is necessary. Providing the boundary values with local smoothing was insufficient to maintain free exchange of mass and energy across the interfaces. This can be seen in Fig. 15b, which shows the reflections of the U-component from the east interface. A method suggested by Madala (1977), which consisted of calculating the mass convergence of the coarse mesh at the interface to provide values for certain boundary fine mesh mass flux terms, was attempted without success. (Refer to Appendix B for details of the divergence boundary condition.)

29

Problems arose at the west and north interface walls where
the horizontal flux terms were removed considerably from
the interface. Changing the interface walls to consist only
of the π , T , and ϕ row would have allowed better conser-
vation of divergence between grids. This change, though,
would have entailed changing the flux forms of the advective
terms and considerable indexing changes. Time did not permit
complete testing of this boundary condition.

C. MARCHING PROCESS FOR THE NESTED MODEL

A schematic of the Matsuno-leapfrog time integration
scheme for both the coarse and fine mesh grids is shown in
Fig. 8. Each sequence is 45 minutes in length. This time
sequence applies the Matsuno scheme less often in the fine
mesh, which results in less damping of the high frequency
oscillations. This is in contrast to Chen and Miyakoda
(1974), who used the Euler-backward time step solely, and
Miyakoda and Rosati (1977), who used a time filter (Asselin,
1972) after each time step.

Due to the oscillations generated at the boundaries of
the coarse and fine meshes, it was difficult to evaluate the
above time stepping scheme. Computational modes did not
appear to be significant in the various model cases studied.

V.   DESCRIPTION OF THE
EXPERIMENT AND RESULTS

The main objective in all nested grid models is to show that the nested solution gives results similar to those of a uniform fine mesh. This applies to situations in which the resolution of the coarse mesh grid is inadequate and the fine mesh resolution is sufficient. An attempt was made in this research to obtain a nested fine mesh solution for flow over mountains.

The following is a listing of the three basic models studied in this research.

(1)   Coarse mesh solution:

   a)   without a mountain
   b)   with mountain A
   c)   with mountain B

(2)   Uniform fine mesh solution:

   a)   without a mountain
   b)   with mountain A

(3)   Nested solution:

   a)   without a mountain, one way
   b)   without a mountain, two way
   c)   with mountain A, one way
   d)   with mountain A, two way

Mountain "A" is the case in which the mountain is built completely across the channel, whereas mountain "B" is built only half-way across the channel. Results to 12 hours are compared, due to problems developing after that time.

31

A. COARSE MESH SOLUTION

Hayes (1977) studied the flow over mountains using the same primitive equation model (Monaco, 1975), except he used the full global model and not a channeled version. Some of his results which can be used in comparison are as follows: (a) the mountains interact with the atmospheric flow to induce ridging over the mountains and troughing on the downstream side; (b) damping of small scale features with height; and (c) increasing the grid resolution causes the scale of the velocity component response to decrease, but the magnitude remains about the same when compared to the coarse grid resolution. The grid size that Hayes used for the coarse mesh, 4.5° long by 4.0° latitude, is the same as used by this author.

Prior to testing the channeled model with a mountain, a case was computed without a mountain. This was done to check if the initialization scheme, which used the linear balance equation, was satisfactory for the channeled model. The model was run to 56 hours with the maximum variation in both velocity components not exceeding ± 1 m/sec over the initial values. Some adjustment was expected because the finite difference form of the analytic solution is inexact. The terrain pressure does experience a variation with time (Fig. 3). This is due, as explained in Chapter III, to the integrated mass flux in the north-south direction not being equal to zero. Therefore, other than the pressure variation, the model does appear to be in good balance.

32

Next, a meridional mountain range 18° x 750 m (width by height) extending across the entire channel was considered. Since the distance between grid points in the ξ-direction is 4.5^O, this allows only three grid points at each latitude to represent the mountain. The middle channel U and V components after six hours are shown in Figs. 9A and 9B for three levels. The mountain has developed to half of its height by this time. Upstream, the flow is deflected northward by the mountain and downstream the flow is deflected to the south. At some distance from the mountain both upstream and downstream, variations due to the mountain are less evident. Figure 9B shows an increase in the U-component in the vicinity of the mountain top. The increase can partly be explained by *the use of the conservation of potential vorticity equation,*

$$\frac{\zeta + f}{\Delta p} = \text{constant} ,$$

where ζ is relative vorticity, f is the Coriolis parameter and Δp is the pressure depth of a column. In order to conserve potential vorticity on the upstream side the flow turns anticyclonic and therefore an increase in the V-component results. Over the mountain crest the flow turns cyclonic and the V-component decreases, but due to the decreased column depth the conservation of potential vorticity is achieved by an increase in the U-component.

The vertical velocity field, shown in Fig. 10, indicates rising motion on the upstream side with sinking motion just over the mountain crest and downslope. In addition, a

33

secondary region of rising motion is indicated downstream.
This can be indicative of a mountain lee trough.

The temperature patterns for the middle of the channel
at the six different levels is shown in Fig. 11. Note the
cooling on the upslope side of the mountain and the warming
downstream. This is a direct result of the vertical veloc-
ities induced by the mountain. It must be noted, though,
that the temperature field over the entire channel increased
on the average of $10^{o}K$ at all levels from initial tempera-
tures. This was due in part to term (1) of the equation in
Appendix A, the integrated η-component of momentum and the
imbalance of mass flux terms between the north and south
boundaries.

At 12 hours, the mountain has attained its final height.
The horizontal wind profiles for this time are shown in
Figs. 12A and B. The U-profiles appear reasonable with the
highest zonal velocity over the mountain crest, and also a
decreasing magnitude with height. The V-profiles, though,
begin to show problems. At level six the flow is still being
deflected in the proper way, but problems are appearing at
levels one and three. Although they, too, are showing
proper deflection, the maxima of level one is the same magni-
tude as level six. This is unexpected, based on Hayes'
results showing dampening with height.

The large unexpected maxima at level one is possibly due
to two factors. The first is due to the method of specifying
$\frac{\partial \phi}{\partial \eta}$ at the boundaries (refer to Chapter III for details.)

34

The second is the apparent development of a meridional, vertical oscillation as a result of the vertical velocity pattern induced by the mountains. Note in Fig. 12A the apparent compensating northward flow downstream at level six in response to the southward flow at levels one and three. In Fig. 13 the largest vertical velocities at level five, and, therefore, vertical transport of momentum, are shown to be occurring along the channel walls in the vicinity of the mountain. This pattern of the largest vertical velocities occurring at the channel wall-mountain intersection continues with time and dominates the vertical velocity patterns after 24 hours.

To estimate the effect of the mountain-channel wall intersection, a test case was computed using the half-channel mountain "B". The horizontal velocity profiles were similar to the channeled mountain, except for a slight increase in the zonal flow north of the mountain. The 12 hour vertical velocity pattern, Fig. 14, associated with level five of mountain "B" is slightly different, especially along the north wall, when compared to the pattern of mountain "A", Fig. 13. At 12 hours the largest vertical velocities appeared along both the north and the south walls. Even with the mountain not intersecting the north wall, vertical velocities of the same magnitude as in Fig. 13 developed. Further tests would be required to determine the minimum distance needed to prevent interaction of the flow around the mountain and the channel wall.

B. UNIFORM FINE MESH

The same geographic domain as in the coarse mesh model was used in the fine mesh model with one-third the grid distance. Due to the increase in the computer memory requirements (9X) and CPU (Central Processing Unit) time (27X), associated with this solution, few case studies were completed.

The case in which there was no mountain was computed to evaluate the initial balance and pressure, i.e. mass, variation over the total field. Results through 12 hours showed maximum velocity variations of $\pm$ 1 m/sec. The average pressure over the domain did vary with increases of .3 mb at six hours and 2.6 mb at 12 hours. The phase and period of these pressure oscillations were difficult to calculate as the required long computer runs had to be limited due to the excessive processing times. It appears, though, to have a phase close to that of the coarse grids phase, but a smaller magnitude.

Regrettably, due to time limitations, the uniform fine mesh with a channel mountain was not run for a sufficiently long time to use in this study. Results achieved by Hayes (1977) in increasing the horizontal grid resolution (ξ-direction only) can be used as a basis of what to expect. Mainly, he found that by increasing the resolution in the ξ-direction the velocity component response decreased, but the magnitude of that response remained approximately the same when compared to the coarser resolution grid.

C. NESTED SOLUTION

Two methods of interaction are employed with the nested grid model. The first method is one-way interaction; values from the coarse mesh are supplied to the fine mesh boundary at appropriate times, with no corresponding changes of coarse mesh interior values from the nested fine mesh. The other method is two-way interaction. Although boundary values for the fine mesh are still provided by the coarse mesh, replacement of coarse mesh values by interior nested fine mesh values at coincident points is done at appropriate times. For example: v(I+3,J+2) of fine mesh replaces v(I+2, J+2) of coarse mesh. A five point averaging scheme surrounding each fine mesh coincident point is used to calculate the replacement fine mesh value.

Prior to testing the nested grid with a mountain present, one case with each type of interaction was run without a mountain to check the initial balance. As mentioned in section 1 of this chapter, the coarse mesh is in good balance. The v and u components in the middle region of the fine mesh after six hours are shown in Figs. 15A and B. The corresponding coarse mesh solution can be seen at either end of each plot. The v-component profile shows level $1(\sigma = .08)$ to have the largest value. This can be due to the following: 1) the oscillations of the height surfaces in the north-south direction forced by the coarse mesh boundary values, 2) the interface boundary conditions, and 3) the phase differences in pressure oscillations. The u-component profile,

Fig. 15B, shows the reflection of energy from the east wall. Insufficient interface boundary conditions did not allow free exchange of mass and energy across the interface, thereby resulting in the reflections.

In addition, Fig. 5 shows the pressure variations for the nested (one-way) fine mesh. These oscillations appear to follow the variations of the 1.5° uniform fine mesh (nested domain) spacing out to eight hours. After that time, the coarse mesh variations force the nested variations. This could lead to imbalances.

When the two-way interaction scheme is used, the fine mesh has significant influence on the coarse mesh, Fig. 16. In one-way interaction the coarse mesh v-profile would show only a +.5 m/sec value for the three levels. It should be noted, though, that the variations of the fine mesh horizontal velocity components were not as large in the two-way as in the one-way. This was due to the transfer of energy out of the nested grid into the coarse grid. This allowed any oscillations present in the fine mesh region to propagate to the coarse mesh region. These oscillations, though, aggravated the problems at the coarse mesh boundary wall. From 12 hours and beyond, the oscillations in both grids become unrealistically large.

The last series of experiments was computed using the nested, two-way interacting model with a 18° x 750 m mountain present. This allows three grid points in the coarse mesh and 11 grid points in the fine mesh to represent the mountain at each latitude. The resulting horizontal velocity profiles

38

after six hours for the fine and coarse meshes are shown in Figs. 17 and 18. The mountain has developed to half its height by this time. The v-profiles in Fig. 17A show the general upstream northward deflection and downstream southward deflection. In addition, the upstream flow appears to be deflected northward only in the immediate vicinity of the mountain. This is different than the coarse mesh solution which shows deflections three gird points upstream from the mountain. This narrowing of the velocity component response compares favorably with that of Hayes (1977). One result which does not compare is the lack of dampening with height. This is probably a result of the improper v-component values from the coarse mesh being forced at the nested boundary interface.

The u-profile (Fig. 17B), for level $6(\sigma = .92)$ does indicate an increase in the zonal flow over the mountain top, and then a return to the upstream value. The upper two levels $(\sigma = .42, .08)$, though, show an increase in the zonal flow downstream of the mountain. This is probably caused by the reflections from the east interface wall.

The coarse mesh velocity profiles are shown in Figs. 18A and B. When compared to Figs. 9A and B, the one-way interacting mountain case, few significant differences are noticed. The v-profiles show the proper deflection north and southward, with the zonal flow increasing in the region of the mountain top. Since the flow in the region of the mountains is just an average of the nested region flow, the fine mesh solution must have been good for the first six hours.

In Figs. 19 and 20 are shown the v-component profiles
and vertical velocities for the coarse mesh at 12 hours.
The v-profiles show a large level 1(σ = .08) northward com-
ponent with a compensating lower level 6(σ = .92) southward
component. The fine mesh v-profile is similar, except the
deflections are spread wider over its domain. Part of the
reason for the large upper level v-component is the inter-
action of the mountain and the channel walls. As mentioned
in section 1, large vertical velocities are created at the
intersection with channel wall points, which causes an
artificial meridionally oriented, vertical circulation. The
same circulation apparently occurs in the fine mesh, due to
interface, mountain intersection. This energy is then par-
tially transferred to the coarse mesh via the two-way inter-
action. The coarse mesh vertical velocities are shown in
Fig. 20. The fine mesh influence is immediately apparent.
By this time, the solutions to the nested grid model are
dominated by unrealistic oscillations. Similar results were
obtained in the one-way interaction solutions.

VI.   SUMMARY AND CONCLUSIONS

This thesis was undertaken to study the flow over moun-
tains using a channeled model with an interior nested grid.
The work involved two stages. The first was to develop an
east-west channel model from a global model. The second was
the nesting of a finer resolution grid.

In channeling the modified Arakawa global model by
Monaco and Williams (1975), oscillations and noise arose
along the channel walls. The scheme C grid arrangement and
flux form of the advective terms lead to certain boundary
conditions. These proved to be adequate when no disturbance
was present, but insufficient when either a mountain and/or
nested grid were introduced. Difficulties also arose at the
mountain-channel wall intersection.

In nesting a finer resolution grid several things were
learned. The numerical response in the ξ-direction decreases
with the finer resolution when compared to the coarse mesh
solution. In addition, the two-way interaction does allow
partial transfer of energy to the coarse mesh. Several prob-
lems were also encountered.

The grid arrangement and flux form of advective terms
lead to similar boundary/interface conditions as in the
coarse mesh. Difficulties did not arise at the interface
walls due to extrapolation methods in providing boundary
values, but they resulted due to not allowing free exchange

41

of energy and mass across the interface walls. This caused internal reflected fine mesh waves, which eventually destroyed the fine mesh solution. The mountain-interface wall intersection also accounted for some of the problems. As in the coarse mesh, large vertical velocities developed at these intersection points, which are partly responsible for the vertical meridional oscillations.

Based on the above results, the following is recommended:

(a) expand the channel in the north-south direction sufficiently to allow isolating the mountain. This would avoid the problems caused by the mountain channel wall intersection;

(b) simplify the flux forms in the primitive equations for use over the whole domain;

(c) modify the channel walls to consist of one latitude ϕ , t , u row. This leads to an unequal predictive region for the v-component;

(d) modify the interface walls in the nested grid to consist of one latitude (north and south walls) and one longitude (east and west walls) row. This leads to unequal predictive rows for v and u-components, respectively;

(e) alter linear interpolation scheme to higher order scheme for providing the nested grid boundary with coarse mesh values.

Although this thesis was not entirely successful in mathematically simulating flow over mountains, it did identify and detail some specific problems. It is hoped that this study will prove useful to those attempting a similar study in the future.

42

APPENDIX A

NORTH AND SOUTH BOUNDARY CONSIDERATIONS

The constraint of no net mass flux in the north-south
direction is a primary factor to consider when determining
boundary conditions for the north and south walls. Due to
the cyclic condition in the east-west direction, the only
equation of motion needed to be considered is equation (2-3),
the v-component equation:

$$\frac{\partial}{\partial t}(\frac{\pi}{mn}\ v) + \frac{\partial}{\partial \xi}(\frac{\pi u}{n}\ v) + \frac{\partial}{\partial \eta}(\frac{\pi v}{m}\ v) + \frac{\partial}{\partial \sigma}(\frac{\pi \dot{\sigma}}{mn}\ v)$$

$$(1) \qquad\qquad (2) \qquad\qquad (3) \qquad\qquad (4)$$

$$+ \frac{f \pi u}{mn} + (v\ \frac{\partial}{\partial \xi}\ \frac{1}{n} - u\ \frac{\partial}{\partial \eta}\ \frac{1}{m})\pi u + \frac{\pi}{m}\{\frac{\partial \Phi}{\partial \eta} + \sigma\alpha\ \frac{\partial \pi}{\partial \eta}\} = \frac{\pi}{mn}\ F_\eta\ .$$

$$(5) \qquad\qquad (6) \qquad\qquad\qquad (7) \qquad\qquad (8)$$

To assure no net mass flux, the above equation, integrated
in ξ and σ, must balance.

Following is an analysis of each term, and what must be
done to accomplish the constraint condition.

Term (1):

$$\int_\xi \int_\sigma \frac{\partial}{\partial t}(\frac{\pi}{mn}\ v)d\sigma d\xi = \frac{\partial}{\partial t} \int_\xi \int_\sigma (\frac{\pi v}{mn})d\sigma d\xi = 0$$

In the case where no mountain is present, $\frac{\pi v}{mn}$ starts at
zero and should remain zero as long as the model initiali-
zation is correct. When a mountain is present, there must

43

be a shift of mass to another region in order to satisfy
the integral.

Term (2):

$$\int_{\xi}\int_{\sigma} \frac{\partial}{\partial\xi}\left(\frac{\pi u}{n}\, v\right)d\sigma d\xi = 0$$

This is due to the cyclic condition east-west.

Term (3):

$$\iint_{\xi}\int_{\sigma} \frac{\partial}{\partial\eta}\left(\frac{\pi v}{m}\, v\right)d\sigma d\xi = \int_{\xi}\int_{\sigma} v\,\frac{\partial}{\partial\eta}\left(\frac{\pi v}{m}\right)d\sigma d\xi + \iint_{\xi}\int_{\sigma} \frac{\pi v}{m}\,\frac{\partial v}{\partial\eta}\, d\sigma d\xi$$

The first term on the right hand side is taken care of by
reflecting the normal mass flux quantities along the bound-
aries. In the no mountain case, the second term starts at
zero and remains close to zero as the model advances in time.
When a mountain is introduced, this term becomes non-zero.
This problem is further accentuated by the imbalance in the
pressure gradient term (7).

Term (4):

$$\int_{\xi}\int_{\sigma} \frac{\partial}{\partial\sigma}\left(\frac{\pi\dot{\sigma}}{mn}\, v\right)d\sigma d\xi = 0$$

If $\dot{\sigma} = 0$ at $\sigma = 1$ and $\sigma = 0$, this term is satisfied.

Term (5):

$$\int_{\xi}\int_{\sigma} \frac{f\pi u}{mn}\, d\sigma d\xi \neq 0$$

44

This term is not equal to zero, but will primarily be balanced by the pressure gradient term. The term will further vary if a mountain is present.

Term (6):

$$\int_\xi \int_\sigma (v \frac{\partial}{\partial \xi} \frac{1}{n} - u \frac{\partial}{\partial \eta} \frac{1}{m}) \pi u d\sigma d\xi = \int_\xi \int_\sigma \pi u v \frac{\partial}{\partial \xi} \frac{1}{n} d\sigma d\xi$$

$$- \int_\xi \int_\sigma u^2 \pi \frac{\partial}{\partial \eta} \frac{1}{m} d\sigma d\xi \neq 0$$

The first term on the right hand side starts at zero (v=0), and will remain close to zero as the model advances in time. The second term is not zero, because the integrated scaling factor is non-zero. The contribution, though, is very small compared to the other terms in the equation. Its importance, however, increases as the velocity components increase. Since the other terms are not exactly zero, this term adds to the imbalance.

Term (7):

$$\int_\xi \int_\sigma \frac{\pi}{m} [\frac{\partial \phi}{\partial \eta} + \sigma \alpha \frac{\partial \pi}{\partial \eta}] d\sigma d\xi \neq 0$$

This term is non-zero and primarily balanced by the ξ-component of velocity. In order to prevent mass variations, though, its initial balance along the boundaries must be maintained. The initial terrain pressure gradient was relatively simple to maintain but the initial geopotential height gradient was not so simple.

45

Term (8):

$$\int_{\xi} \int_{\sigma} \frac{\pi}{mn} F_{\eta} \, d\sigma d\xi = 0$$

This model is frictionless.

APPENDIX B

DIVERGENCE BOUNDARY CONDITION

Free exchange of mass and energy across the nested grid interface is a necessity to prevent reflections from the walls destroying the fine mesh solutions. In addition to the two-way interaction scheme, a divergence boundary condition after Madala (1977) was attempted.

This boundary condition entailed calculating the coarse mesh divergence along the interface, and interpolating spatially and temporally to determine the fine mesh mass flux quantity on the outside of the interface. The following formulas were used for the east and south interfaces respectively:

$$(\pi u \, \frac{\Delta \eta}{n})_{I,J} = \text{DIV}_{\text{coarse}} + (\pi u \, \frac{\Delta \eta}{n})_{I-1,J} - (\pi v \, \frac{\Delta \xi}{m})_{I,J+1}$$

$$+ (\pi v \, \frac{\Delta \xi}{m})_{I,J}$$

$$(\pi v \, \frac{\Delta \xi}{m})_{I,J} = -\text{DIV}_{\text{coarse}} + (\pi u \, \frac{\Delta \eta}{n})_{I,J} - (\pi u \, \frac{\Delta \eta}{n})_{I-1,J}$$

$$+ (\pi v \, \frac{\Delta \xi}{m})_{I,J+1} \, .$$

The interface divergence boundary conditions were not applied along the north and west interfaces, due to the problems mentioned in chapter IV. With this boundary condition used

along the east and south walls, results were still unsatisfactory. Reflections were still occurring, indicating a free transfer of mass and energy was not present.

Madala (1977) apparently solved this problem by using weighted extrapolated fine mesh U and V values, along with coarse mesh values, in determining the mass flux divergence terms for the fine mesh boundary. This modified the forcing of the coarse mesh divergence fields at the interface. It should be noted that Madala used only the π , T , and ϕ row of the scheme C grid for the boundary. In addition, he used a simplified flux form, thereby he did not need to specify as many external boundary points. This makes the north and west interface conditions exactly the same as the east and south, whereas in this research they would have been different.

k=0	P_t	TROPOPAUSE	$\sigma=.00$ $\dot\sigma=0.0$
	$\dot VT\Phi$	level 1	$\sigma=.08$
	$\dot\sigma$		$\sigma=.17$
	$\dot VT\Phi$	level 2	$\sigma=.25$
	$\dot\sigma$		$\sigma=.33$
	$\dot VT\Phi$	level 3	$\sigma=.42$
	$\dot\sigma$		$\sigma=.50$
	$\dot VT\Phi$	level 4	$\sigma=.58$
	$\dot\sigma$		$\sigma=.67$
	$\dot VT\Phi$	level 5	$\sigma=.75$
	$\dot\sigma$		$\sigma=.83$
	$\dot VT\Phi$	level 6	$\sigma=.92$
k=K+1	P_s	SURFACE	$\sigma=1.0$ $\dot\sigma=0.0$

Figure 1. The sigma (σ) coordinate system as used in the 6 level model. P_t is 200 mb.
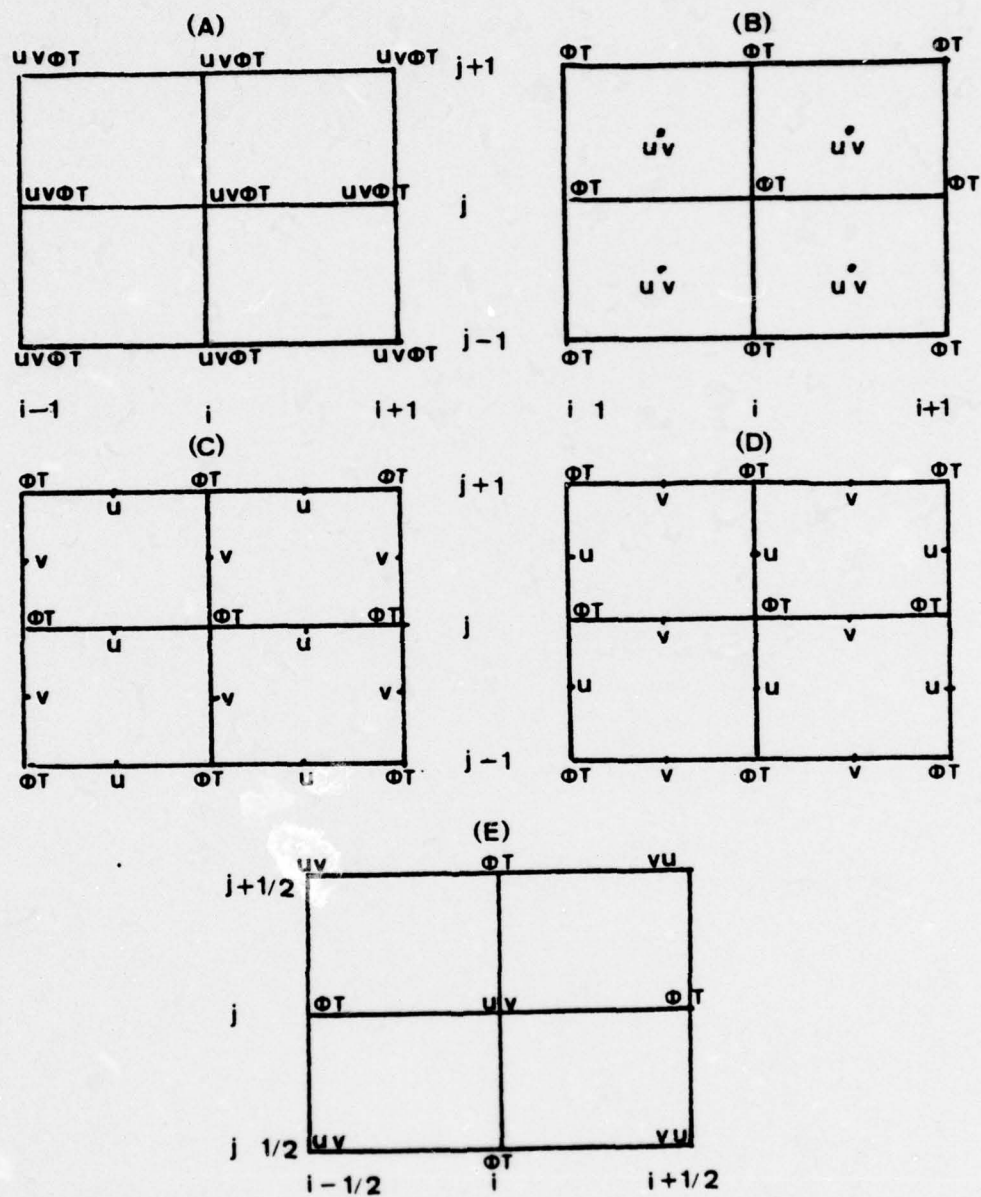
Figure 2. Five possible grid distributions of the dependent variables Φ, T, V, U (after Arakawa, 1974).
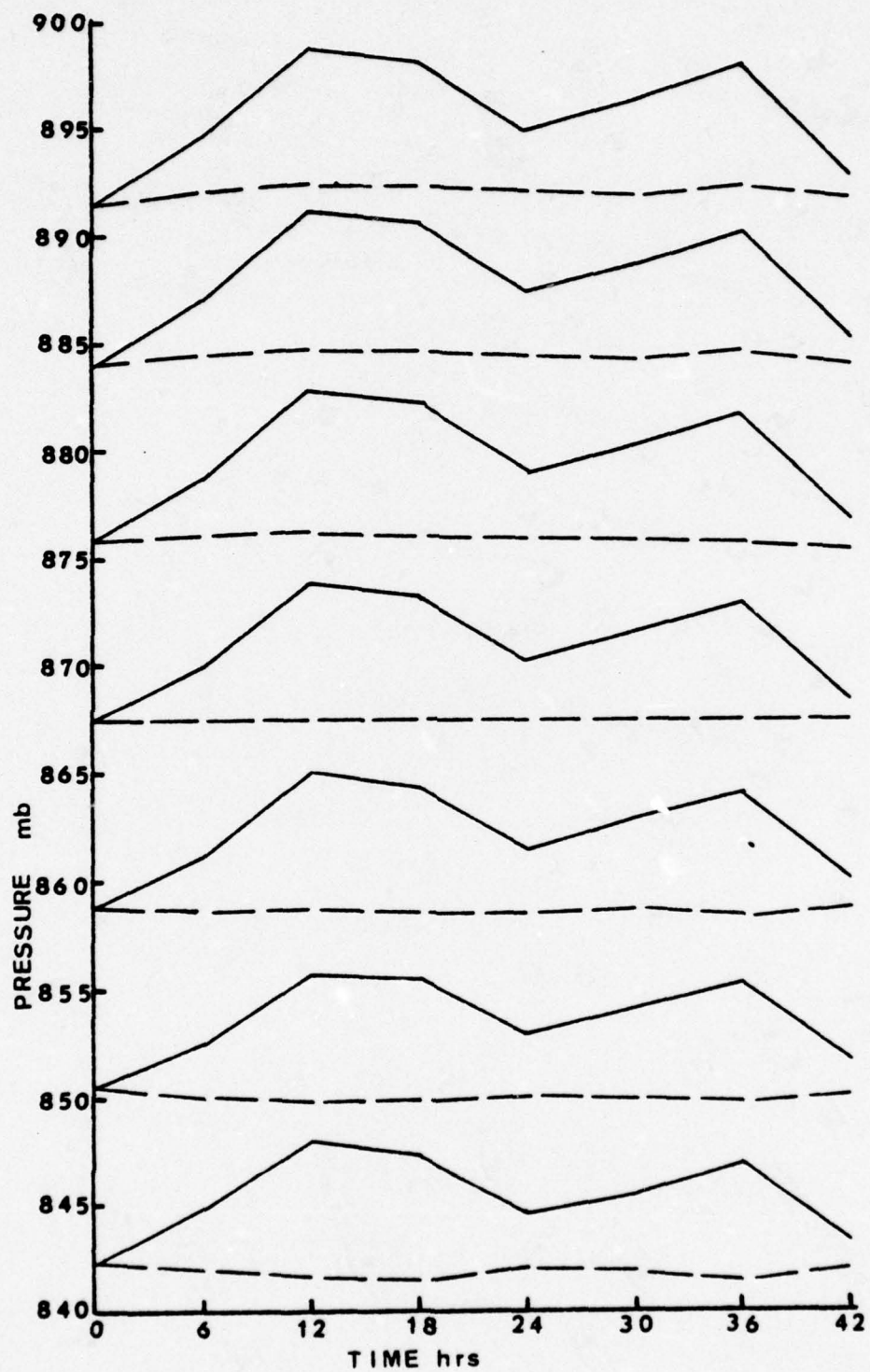
Figure 3.   Pressure variations of the coarse mesh.
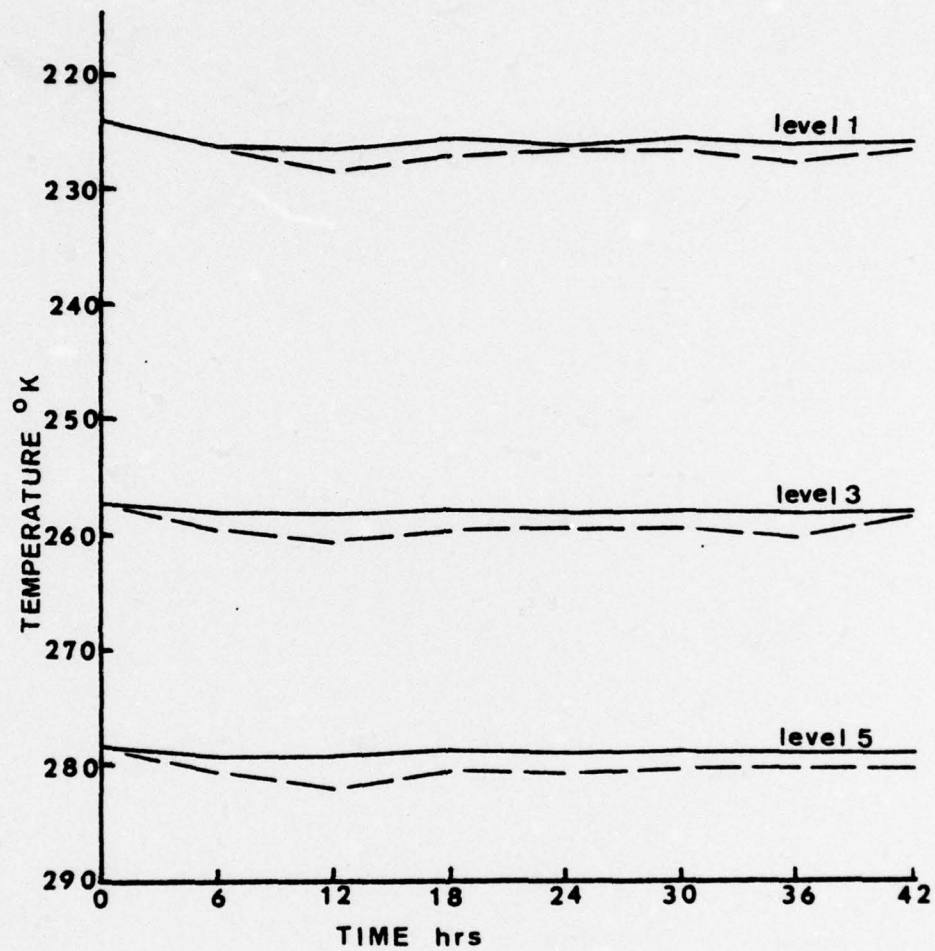
———— w/o (P-$\overline{\Delta P}$)

— — — with (P-$\overline{\Delta P}$)

Figure 4. Temperature variations of the coarse mesh.

——— w/o $(P-\overline{\Delta P})$

— — — with $(P-\overline{\Delta P})$

52
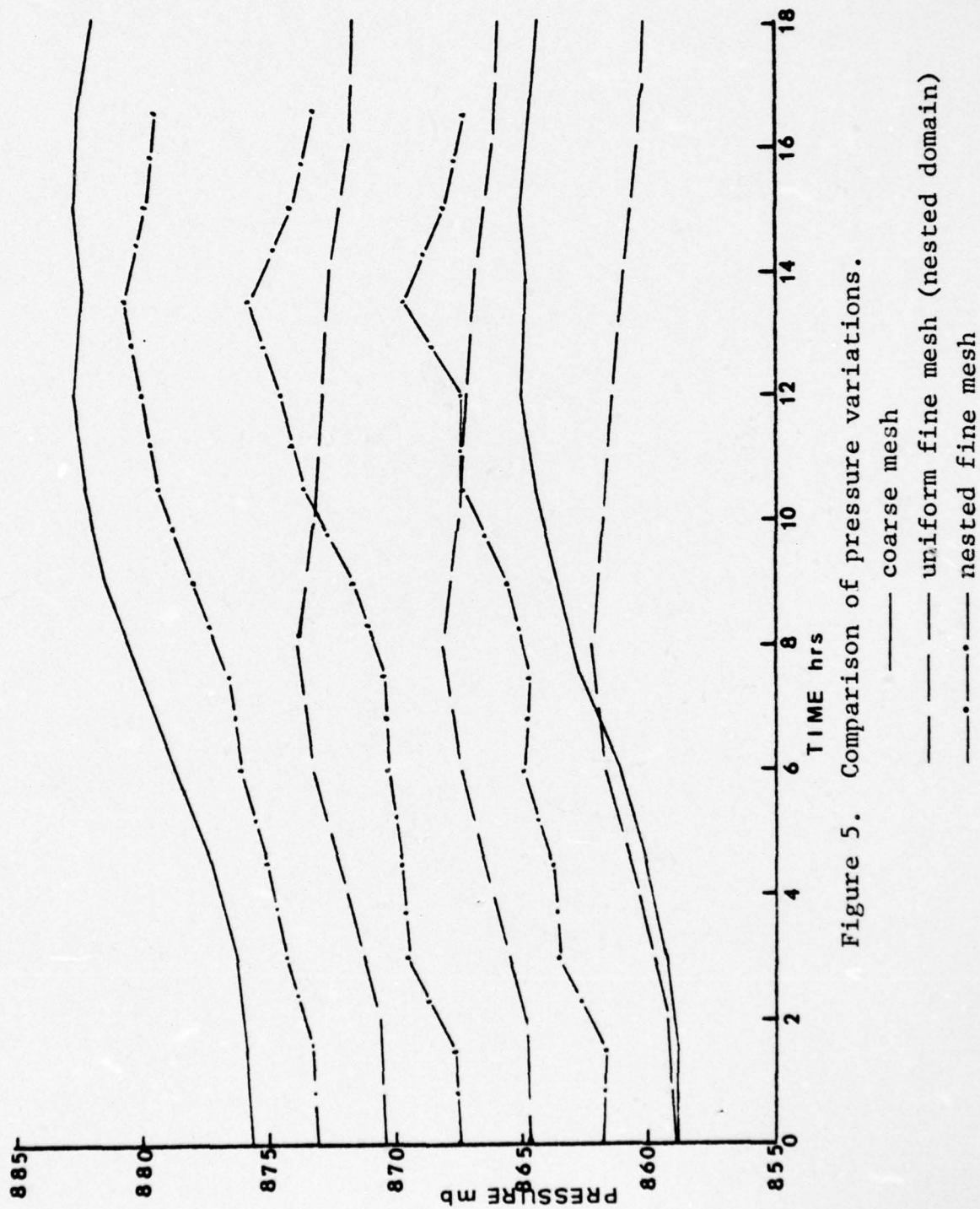
Figure 5. Comparison of pressure variations.

——— coarse mesh

— — — uniform fine mesh (nested domain)

—·—·— nested fine mesh

J=JMAX+1   (πV)   (πV)   (πV)

J=JMAX   φπT   U   φπT   U   φπT   U   } WALL

                   V   V   V

J=JMAX-1   φπT   U   φπT   U   φπT   U

                   V   V   V

            I   I+1   I+2
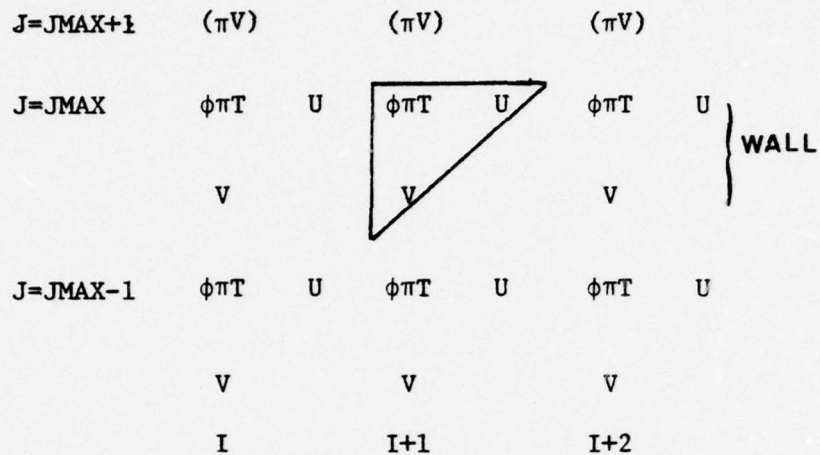
Figure 6A.   North channel wall of coarse mesh.

J=2   φπT   U   φπT   U   φπT   U

                   V   V   V

J=1   φπT   U   φπT   U   φπT   U   } WALL

                   V   V   V

J=0   (πU)   (πU)   (πU)

            I   I+1   I+2
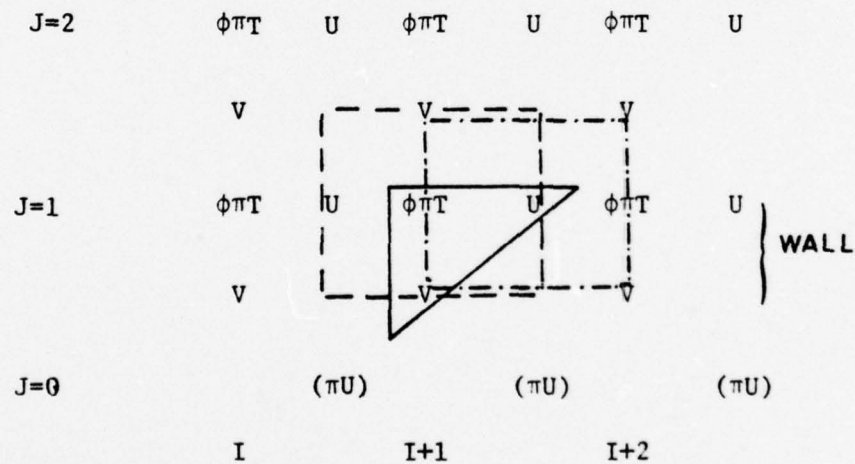
Figure 6B.   South channel wall of coarse mesh.

—— —— ——   simplified mass flux for temperature

——·——·——   simplified mass flux for U-component
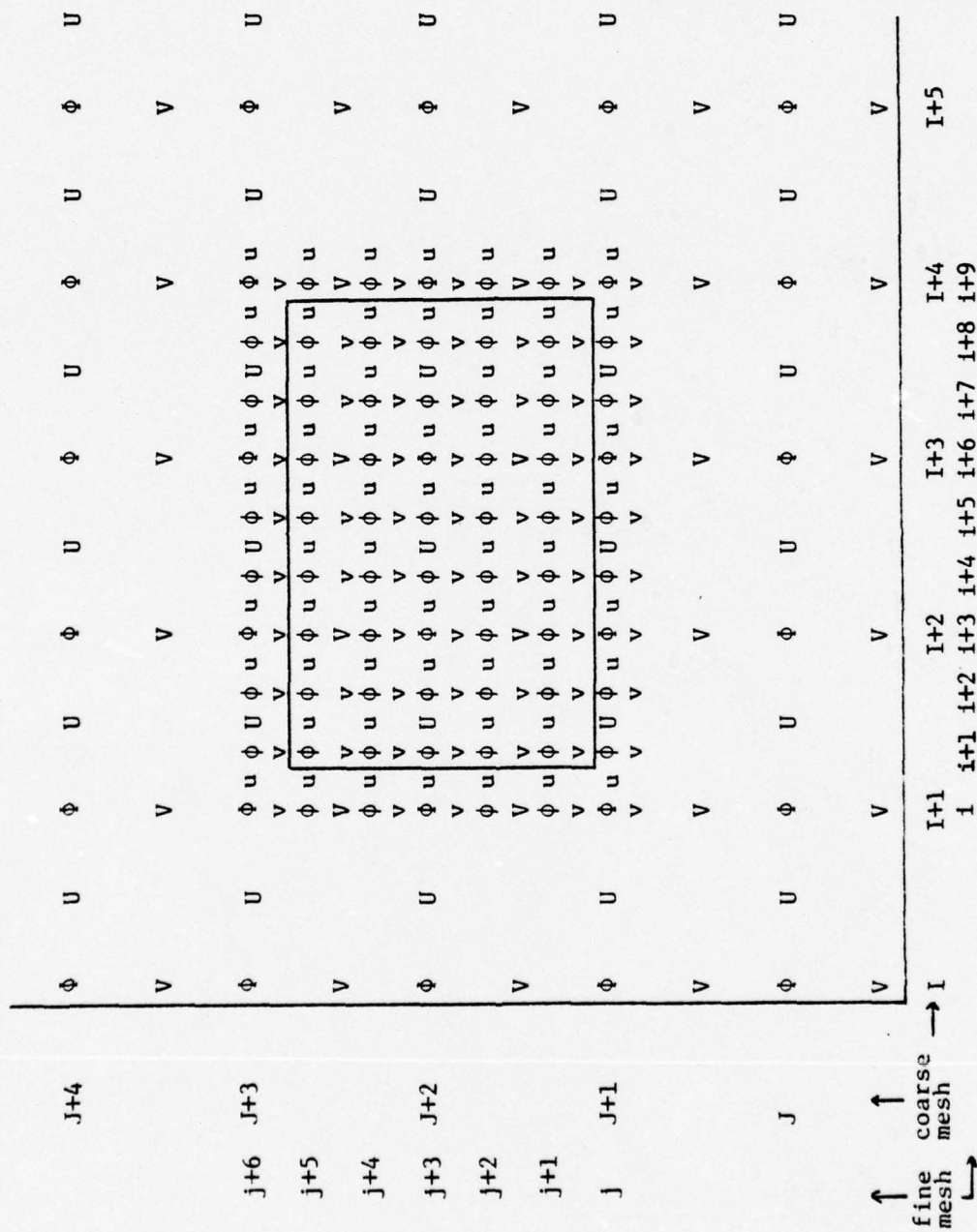
Figure 7. Nested grid system.
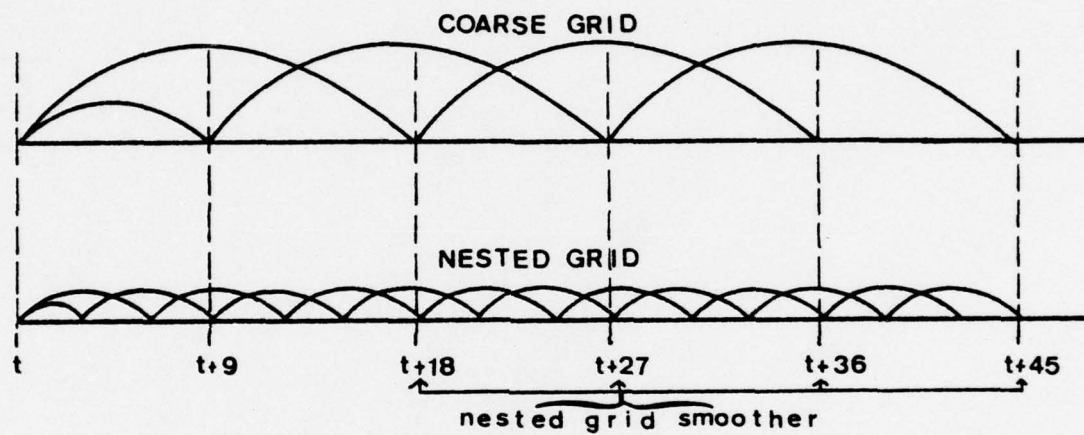
Figure 8. Time step routines for a 45 minute sequence.
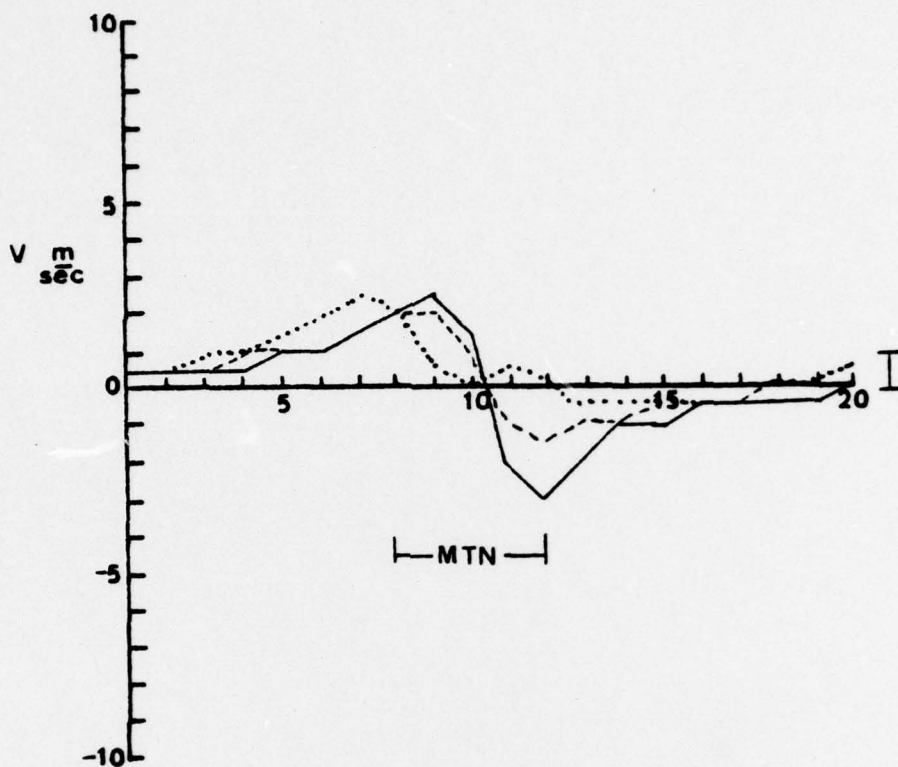
Figure 9A. V-components for coarse mesh with mountain A.
time = 6 hours
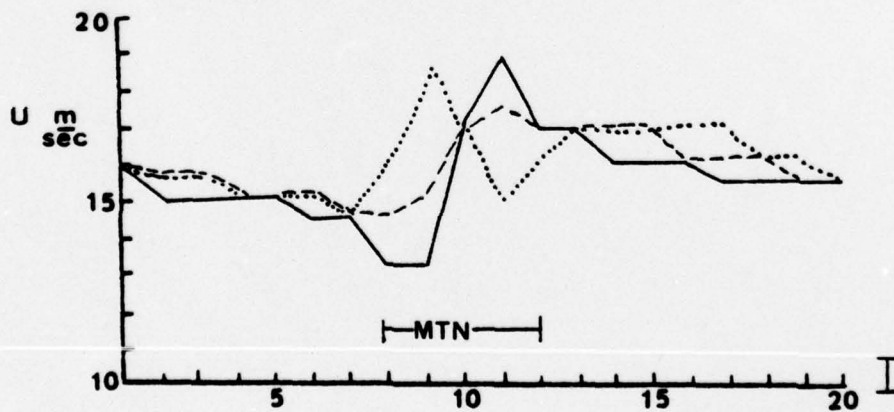
Figure 9B. U-components for coarse mesh with mountain A.
time = 6 hours

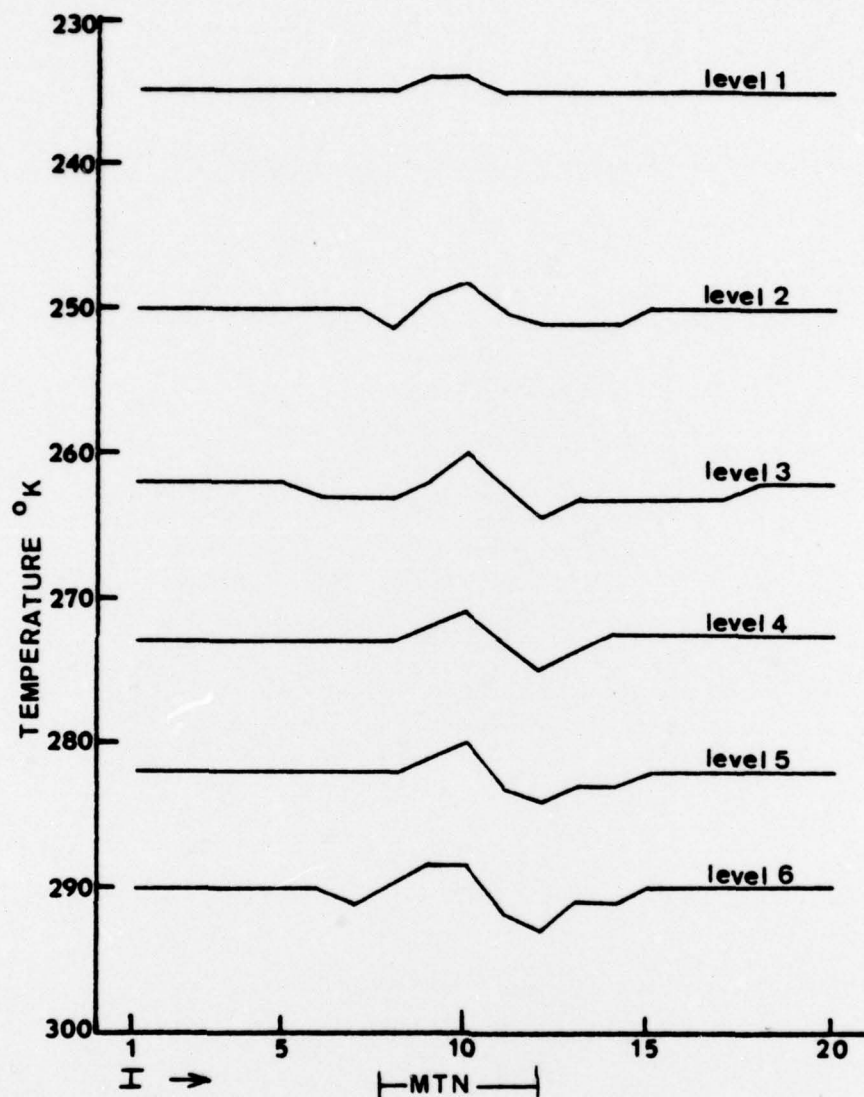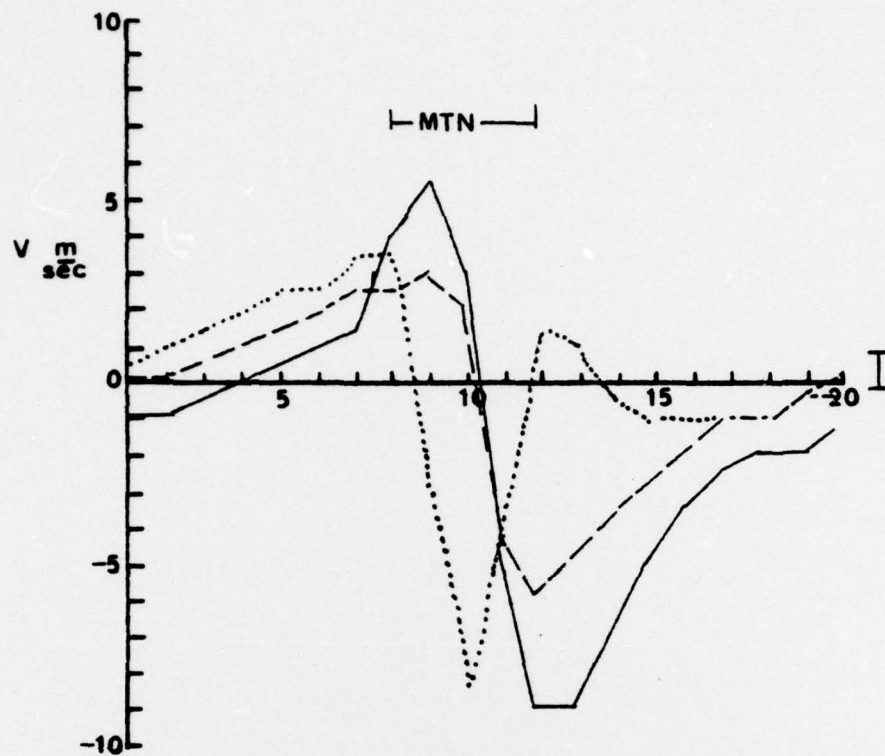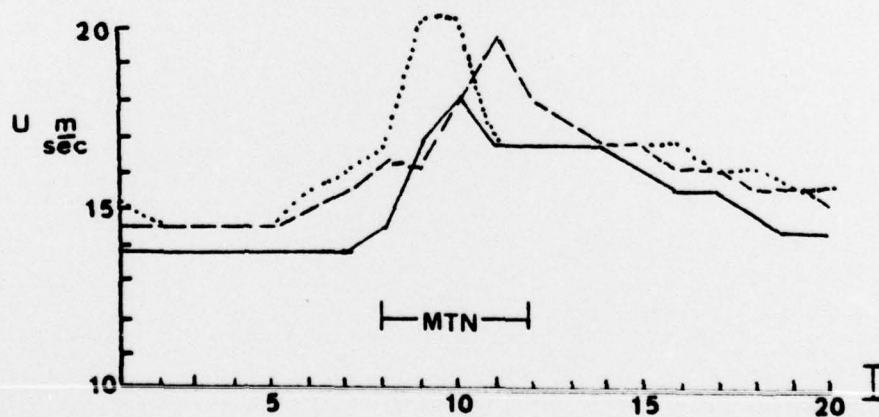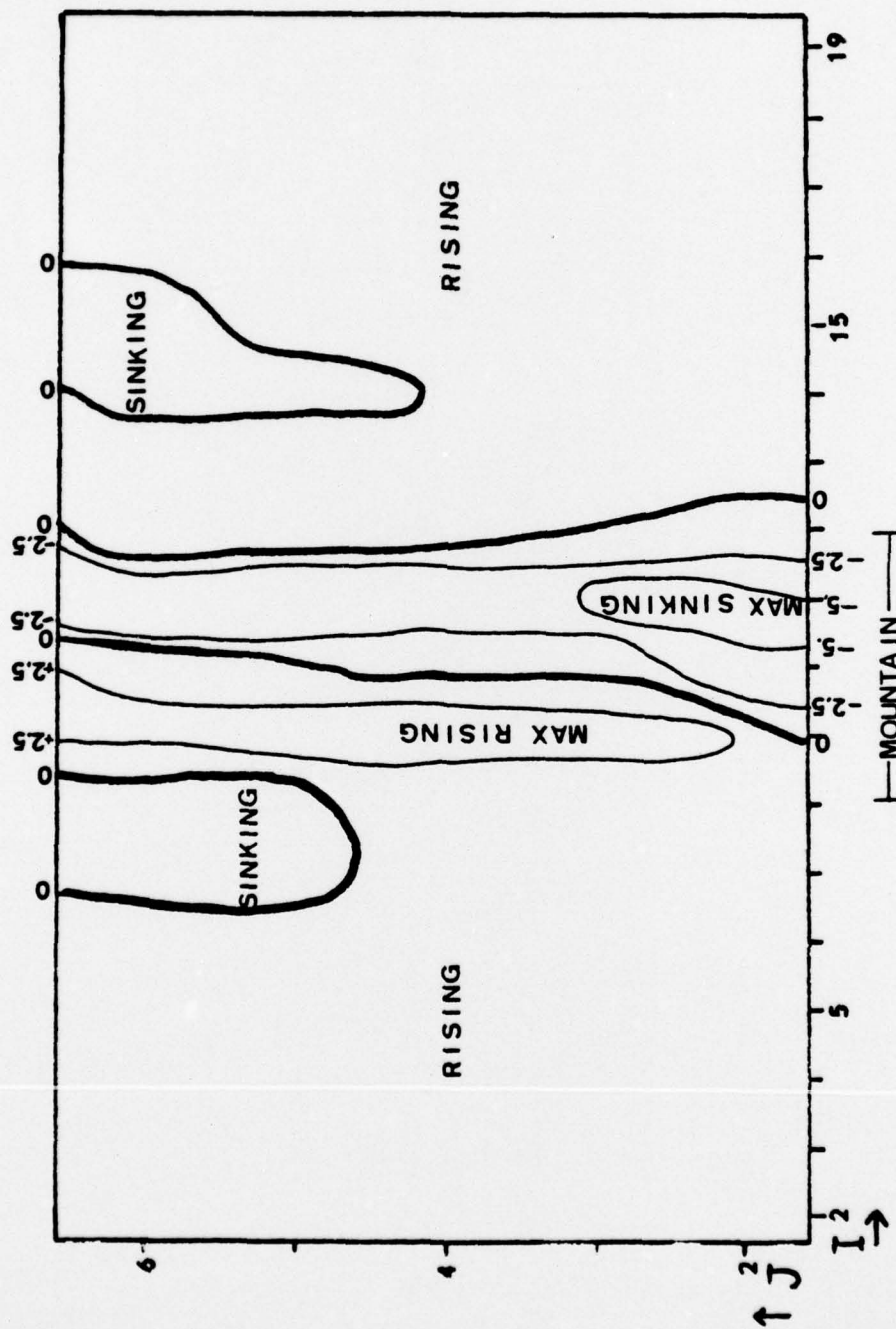σ = .08 (solid line)   σ = .42 (dashed line)
σ = .92 (dotted line)

57

Figure 10. Vertical velocity $(\frac{mb}{hr})$ profile for coarse mesh with mountain A at level 5 (σ = .92). time = 6 hours

Figure 11. Temperature profiles for the six levels of
the coarse mesh model with mountain A.
time = 6 hours

Figure 12A.   V-components for coarse mesh with mountain A.
time = 12 hours

Figure 12B.   U-components for coarse mesh with mountain A.
time = 12 hours

σ = .08 (solid line)   σ = .42 (dashed line)
σ = .92 (dotted line)

60

Figure 13. Vertical velocity ($\frac{mb}{hr}$) profile for coarse mesh with
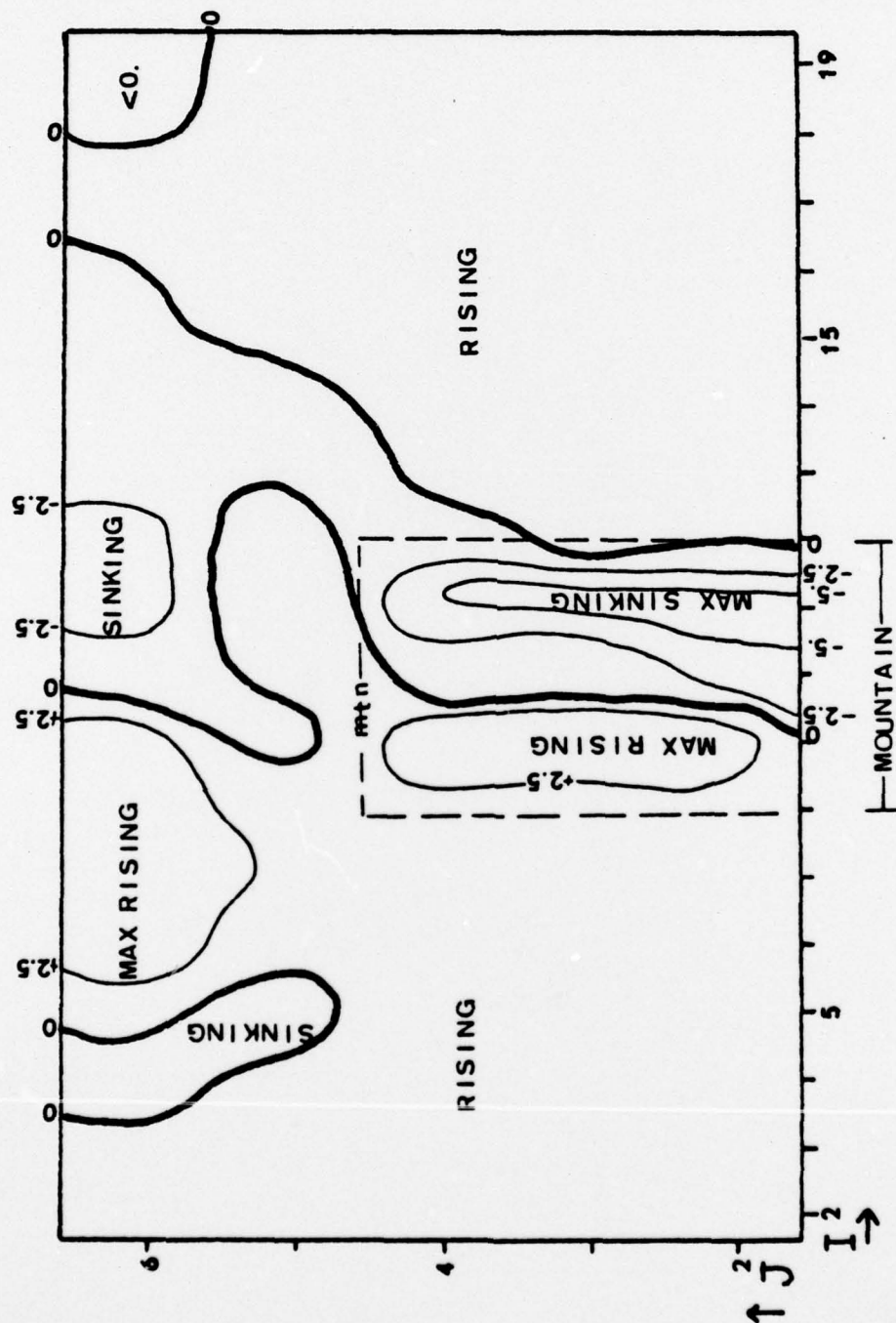mountain A at level 5 (σ = .92).
time = 12 hours

61

Figure 14. Vertical velocity ($\frac{mb}{hr}$) profile for coarse mesh with mountain B at level 5 ($\sigma = .92$). time = 12 hours
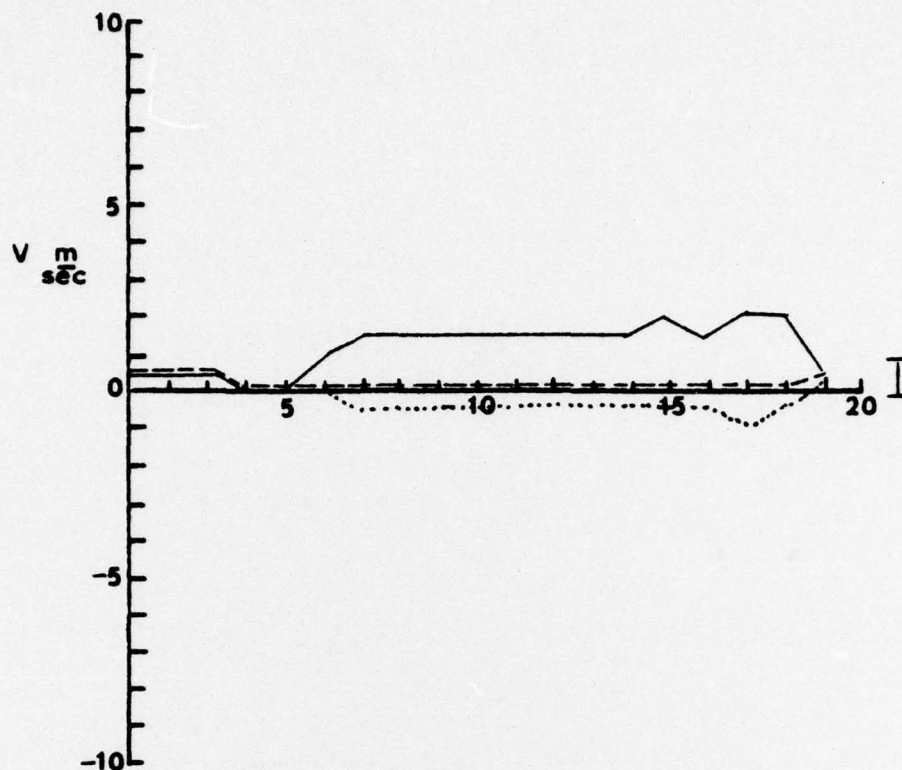
62

Figure 15A. V-components for fine mesh (one-way) with no
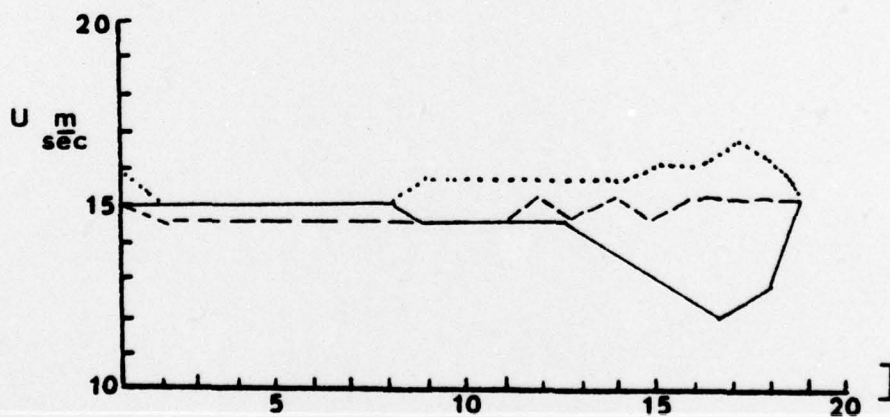mountain.
time = 6 hours

Figure 15B. U-components for fine mesh (one-way) with no
mountain.
time = 6 hours
σ = .08 (solid line) σ = .42 (dashed line)
σ = .92 (dotted line)

63
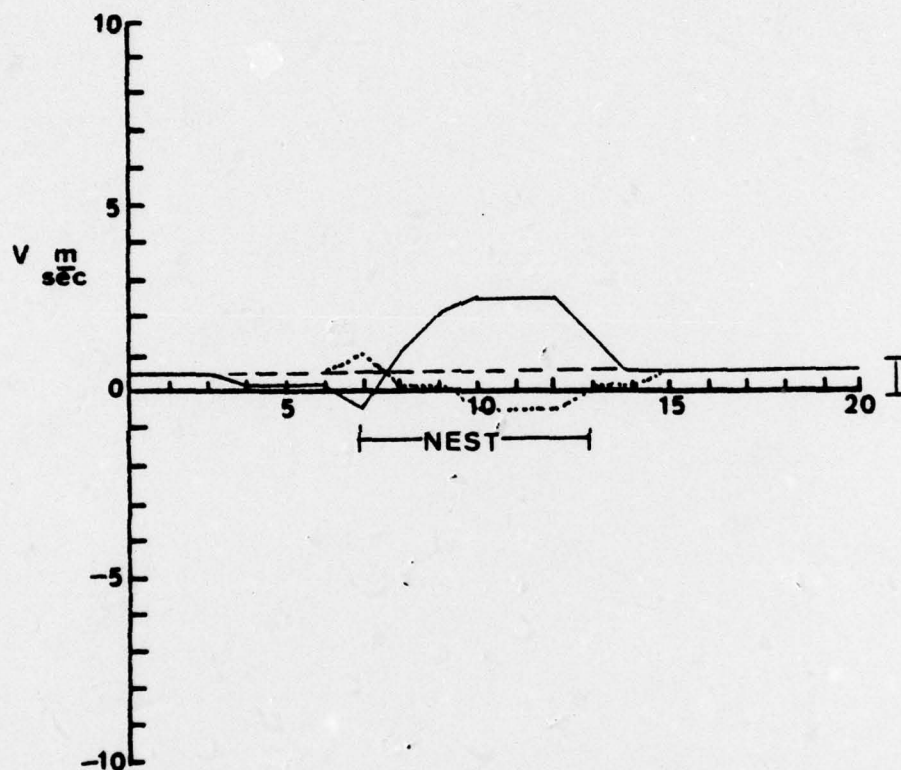
Figure 16. V-components for coarse mesh (two-way) with
no mountain.
time = 6 hours
σ = .08 (solid line)   σ = .42 (dashed line)
σ = .92 (dotted line)
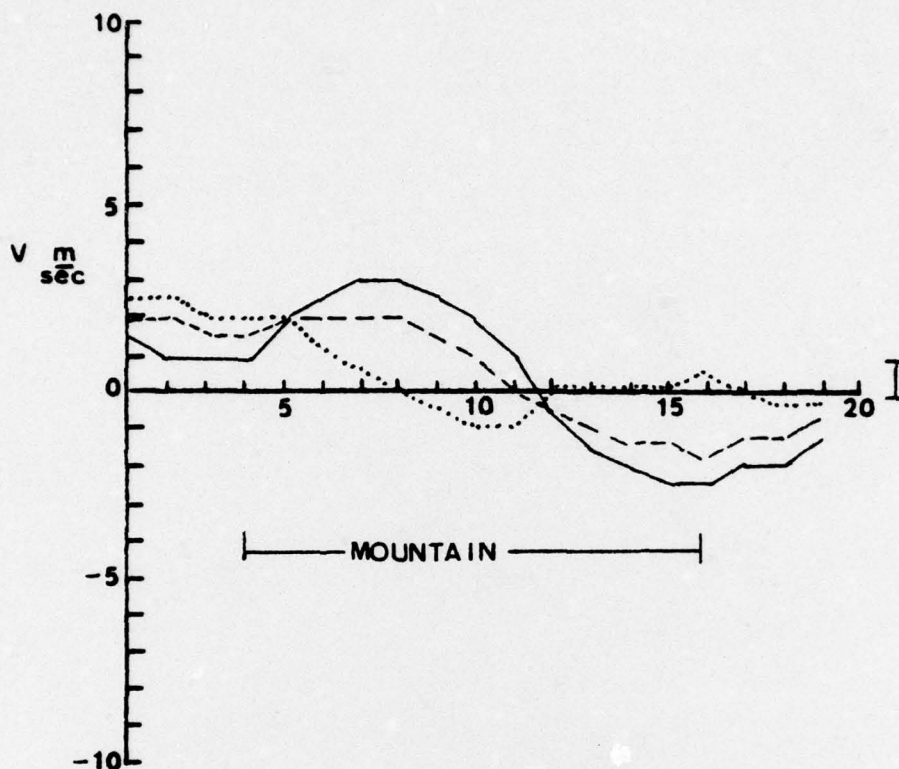
Figure 17A.   V-components for fine mesh (two-way) with
              mountain A.
                    time = 6 hours

Figure 17B.   U-components for fine mesh (two-way) with
              mountain A.
                    time = 6 hours
              σ = .08 (solid line)   σ = .42 (dashed line)
                          σ = .92 (dotted line)

65

Figure 18A. V-components for coarse mesh (two-way) with
            mountain A.
                time = 6 hours

Figure 18B. U-components for coarse mesh (two-way) with
            mountain A.
                time = 6 hours
            σ = .08 (solid line) σ = .42 (dashed line)
                    σ = .92 (dotted line)

66

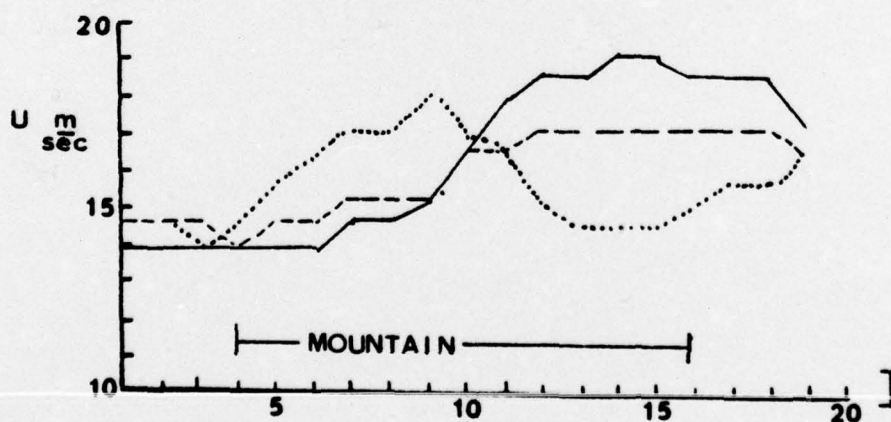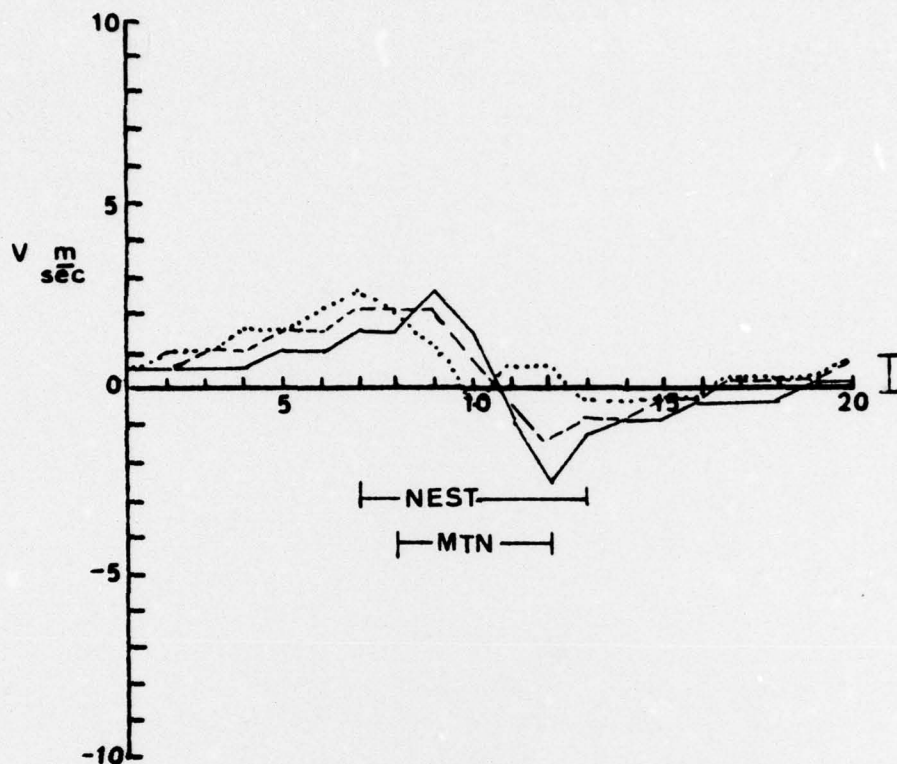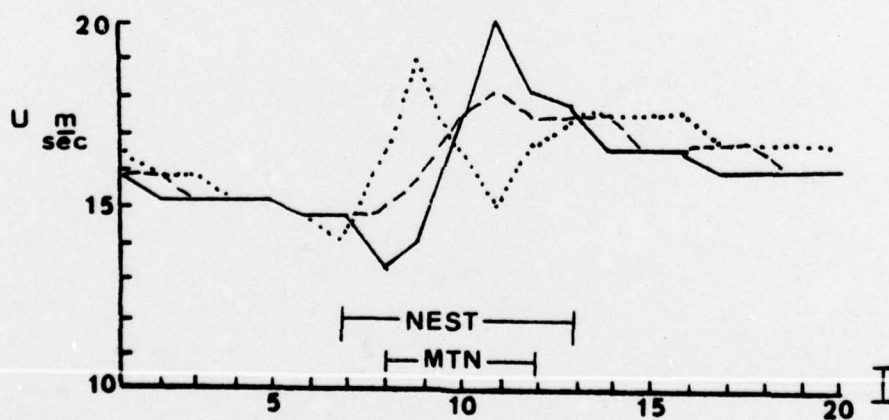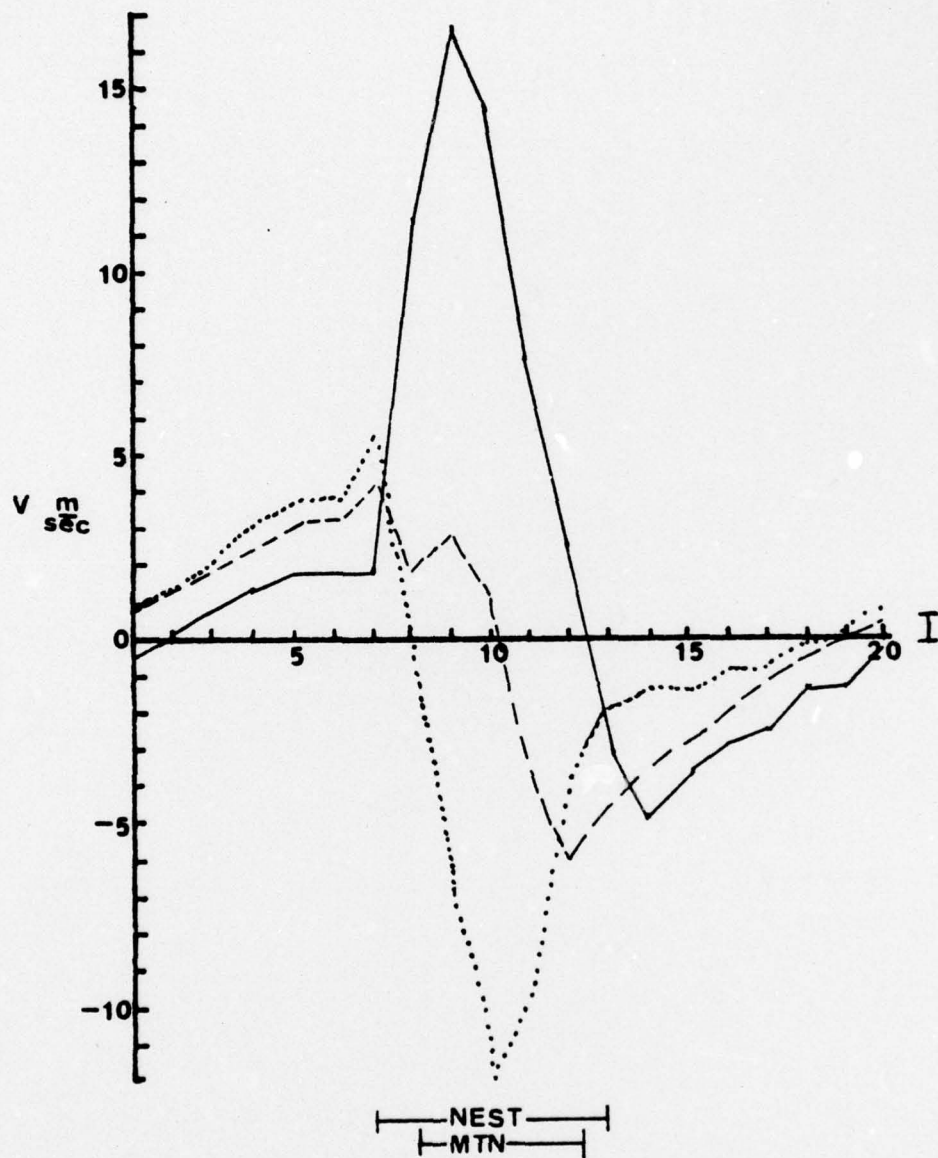Figure 19. V-components for coarse mesh (two-way) with
            mountain A.
                 time = 12 hours
            σ = .08 (solid line) σ = .42 (dashed line)
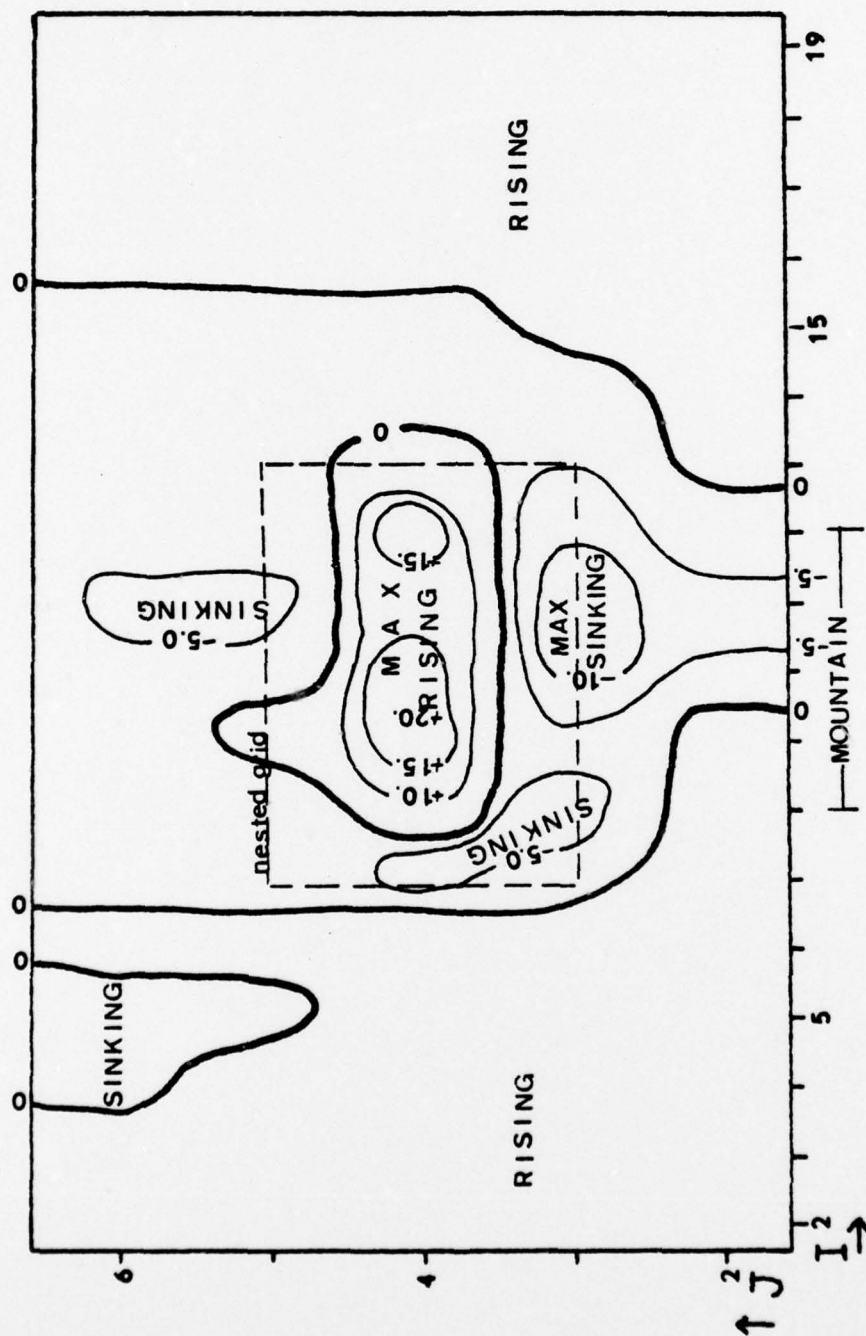 σ = .92 (dotted line)

67

Figure 20. Vertical velocity ($\frac{mb}{hr}$) profile for coarse mesh (two-way) with mountain A at level 5 (σ = .92). time = 12 hours

REFERENCES

Arakawa, A. and Mintz, Y., "The UCLA General Circulation
    Model," workshop notes, I-VIII, Department of Meteorology,
    UCLA, 25 March 1974.

Asselin, R., "Frequency Filter for Time Integrations,"
    Monthly Weather Review, 100, No. 6, pages 487-490,
    June 1972.

Chen, J. H., "Numerical Boundary Conditions and Computational
    Modes," Journal of Computational Physics, 13, pages 522-
    535, 1973.

Chen, J. H., and Miyakoda, K., "A Nested Grid Computation
    for the Barotropic Free Surface Atmosphere," Monthly
    Weather Review, 102, No. 2, pages 181-190, February 1974.

Haltiner, G. J., and Martin, F. L., Dynamical and Physical
    Meteorology. McGraw-Hill, pages 52, 53, 1957.

Harrison, E. J., Jr., and Elsberry, R. L., "A Method for
    Incorporating Nested Finite Grids in the Solution of
    Systems of Geophysical Equations," Journal of Atmospheric
    Sciences, V. 29, pages 1235-1245, October 1972.

Harrison, E. J., Jr., "Three-Dimensional Numerical Simula-
    tions of Tropical Systems Utilizing Nested Finite Grids,"
    Journal of Atmospheric Sciences, V. 30, pages 1528-1543,
    November 1973.

Haurwitz, B., "The Motion of Atmospheric Disturbances on
    Spherical Earth," Journal Marine Research (Sears Founda-
    tion), e, pages 254-267, 1940.

Hayes, J. L., Numerical Simulation of Air Flow over Mountains,
    M. S. Thesis, Naval Postgraduate School, Monterey,
    California, 1977.

Jones, R. W., Integration of a Tropical Cyclone Model on a
    Nested Grid, NOAA Technical Memorandum ERL WMPO-30,
    37 pp, June 1976.

Madala, R. (Personal communication), U. S. Naval Environmental
    Prediction Research Facility, Monterey, California, 93940,
    1977.

Miyakoda, K. and Rosati, A., "One-Way Nested Grid Models: The Interface Conditions and the Numerical Accuracy," (to be published).

Monaco, A. V. and Williams, R. T., 1975: An Atmospheric Global Prediction Model Using a Modified Arakawa Differencing Scheme. Naval Postgraduate School report, NPS-51Wu 75041, 86 pages.

Moss, M. S. and Jones, R. W., Results from a One Dimensional Nested Grid Numerical Model (Part II), NOAA Technical Memorandum ERL WMPO-5, 42 pages, August 1973.

Ookochi, Y., "A Computational Scheme for the Nesting Fine Mesh in the Primitive Equation Model," Journal of Applied Meteorology, 9, pages 545-553, February 1972.

Phillips, W. A., "Numerical Integration of the Primitive Equation on the Hemisphere," Monthly Weather Review, pages 333-345, 1959.

Reiter, E. R., Digest of Selected Weather Problems of the Mediterranean. NAVWEARSCHFAC Tech. paper no. 9-71, April 1971.

Winninghoff, F. J., On the Adjustment towards a Geostrophic Balance in a Simple Primitive Equation Model with Application to the Problems of Initialization and Objective Analysis, Ph.D. Thesis, Department of Meteorology, University of California, Los Angeles, 1968.

INITIAL DISTRIBUTION LIST

No. Copies

1. Defense Documentation Center   2
   Cameron Station
   Alexandria, Virginia 22314

2. Library, Code 0142   2
   Naval Postgraduate School
   Monterey, California 93940

3. Dr. G. J. Haltiner, Code 63Ha   1
   Chairman, Department of Meteorology
   Naval Postgraduate School
   Monterey, California 93940

4. Dr. R. L. Elsberry, Code 63Es   2
   Department of Meteorology
   Naval Postgraduate School
   Monterey, California 93940

5. Dr. R. T. Williams, Code 63Wu   1
   Department of Meteorology
   Naval Postgraduate School
   Monterey, California 93940

6. Lieutenant Stephen M. Schrobo   3
   Naval Weather Service Facility
   NAS, North Island
   San Diego, California 92135

7. Mr. Tom Rosmond   1
   U. S. Naval Environmental Prediction
      Research Facility
   Monterey, California 93940

8. Captain John L. Hayes   1
   Air Force Global Weather Central
   PSC #2, Box 7141
   Offutt AFB, Nebraska 68113